3D early embryogenesis image filtering by nonlinear partial differential equations

Z. Krivá [a], K. Mikula [a], N. Peyriéras [b], B. Rizzi [c], A. Sarti [c,*], O. Stašová [a]

[a] *Department of Mathematics, Slovak University of Technology, Radlinského 11, 813 68 Bratislava, Slovak Republic*

[b] *CNRS-DEPSN, Institut de Neurobiologie Alfred Fessard, Batiment 32-33, Avenue de la Terrasse, 91198 Gif sur Yvette, France*

[c] *DEIS, University of Bologna, Via Risorgimento 2, 40136 Bologna, Italy*

Abstract

We present nonlinear diffusion equations, numerical schemes to solve them and their application for filtering 3D images obtained from laser scanning microscopy (LSM) of living zebrafish embryos, with a goal to identify the optimal filtering method and its parameters. In the large scale applications dealing with analysis of 3D+time embryogenesis images, an important objective is a correct detection of the number and position of cell nuclei yielding the spatio-temporal cell lineage tree of embryogenesis. The filtering is the first and necessary step of the image analysis chain and must lead to correct results, removing the noise, sharpening the nuclei edges and correcting the acquisition errors related to spuriously connected subregions. In this paper we study such properties for the regularized Perona-Malik model and for the generalized mean curvature flow equations in the level-set formulation. A comparison with other nonlinear diffusion filters, like tensor anisotropic diffusion and Beltrami flow, is also included. All numerical schemes are based on the same discretization principles, i.e. finite volume method in space and semi-implicit scheme in time, for solving nonlinear partial differential equations. These numerical schemes are unconditionally stable, fast and naturally parallelizable. The filtering results are evaluated and compared first using the Mean Hausdorff distance between a gold standard and different isosurfaces of original and filtered data. Then, the number of isosurface connected components in a region of interest (ROI) detected in original and after the filtering is compared with the corresponding correct number of nuclei in the gold standard. Such analysis proves the robustness and reliability of the edge preserving nonlinear diffusion filtering for this type of data and lead to finding the optimal filtering parameters for the studied models and numerical schemes. Further comparisons consist in ability of splitting the very close objects which are artificially connected due to acquisition error intrinsically linked to physics of LSM. In all studied aspects it turned out that the nonlinear diffusion filter which is called geodesic mean curvature flow (GMCF) has the best performance.

Preprint submitted to Elsevier *17 March 2010*

Key words: nonlinear partial differential equations, image filtering, mean Hausdorff distance, nonlinear diffusion filtering, laser scanning microscopy images

1 Introduction

Understanding biological processes leading to organism formation through cellular division, interaction and differentiation is a fundamental issue for biomedical research. Such a goal requires investigating cell behaviors in vivo. This is a very challenging multidisciplinary approach requiring specific methodologies and tools in different domains including embryo engineering, microscopy imaging and image processing. Recent advances in imaging strategies open the way to *in toto* 4D imaging of live animals with a resolution at the cellular level and enough contrast to allow segmentation of individual cells and subcellular structures. The zebrafish (Danio Rerio) is a vertebrate that has been largely validated as a powerful model for investigations related to human and might soon become a major model organism for pre-clinical drug testing by pharmaceutical industries. Through the ubiquitous expression of fluorescent proteins in the zebrafish embryo, it is possible to label all the cells and perform the time-lapse LSM (laser scanning microscopy) imaging throughout the embryonic development, (Megason & Fraser, 2003). However, the images produced are intrinsically noisy and any further reconstruction requires noise removal by image filtering algorithms.

Designing appropriate filtering methods for removing spurious structures simultaneously preserving the image information is indeed a requirement for further reliable extraction of cell centers (Frolkovič et al., 2007; Drblíková et al., 2007), segmentation of membranes and nuclei (Zanella et al., 2007, 2009; Frolkovič et al., 2007; Drblíková et al., 2007), velocity field extraction and cell tracking (Melani al., 2007), cf. also (Khairy et al., 2008; Dufour et al., 2005; Lin et al., 2005). Solution of such tasks may lead to the cell lineage tree extraction which is an important and challenging problem in developmental biology and for which our approach gives promising results. In addition to the efficiency and precision, the above mentioned methods are computationally much faster when applied to properly filtered image sequences. Thus, image filtering is a necessary first step in the image processing chain. Furthermore, filters have to be designed and their parameters chosen according to the data

* Corresponding author. Tel.: +39 051 20 93091; fax: +39 051 20 93073
Email addresses: `kriva@math.sk` (Z. Krivá), `mikula@math.sk` (K. Mikula), `nadine.peyrieras@inaf.cnrs-gif.fr` (N. Peyriéras), `barbara.rizzi@unibo.it` (B. Rizzi), `alessandro.sarti@unibo.it` (A. Sarti), `stasova@math.sk` (O. Stašová).

characteristics. Principle constraint of the LSM technique is to acquire images with high temporal resolution in order to follow the motion of every single cell in a continuous way. As a drawback, the spatial resolution of the image sequence dramatically decreases with increasing speed of scanning, particularly in a deepness. Due to the physics of the acquisition process, the resolution in the direction normal to the focal planes is always lower than in the focal planes. Therefore some neighboring close points might not be resolved and sometimes the objects as cell nuclei appear connected in the acquired images, while in reality they are certainly surrounded by cell membranes and thus disconnected. An appropriate preprocessing should then also facilitate the recognition of real structures by splitting regions appearing connected but belonging to different objects. Such a goal can be reached by simultaneous smoothing and sharpening, as performed by the generalized mean curvature flow or Perona-Malik type equations.

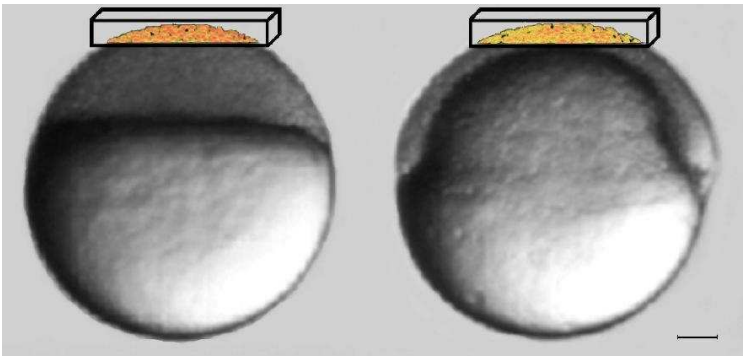

Fig. 1. Zebrafish embryo at the sphere (left) and shield (right) stage. The imaged volume is represented by the volume rendering. Scalar bar: 100μm

We applied methods of nonlinear diffusion filtering to 3D zebrafish embryogenesis images and evaluated their performance with respect to further reliable subcellular structure segmentation. We built fast, accurate and unconditionally stable numerical schemes based on common discretization principles (finite volume method in space and semi-implicit method in time) for several nonlinear diffusion models, including the Perona-Malik equation, and the classical, slowed and geodesic mean curvature flow equations. The partial differential equation (PDE) models are discussed in section 2 and numerical methods are presented and discussed in section 3.

The semi-implicit approach together with finite volume space discretization naturally guarantees unconditional stability and thus robustness of the methods. This property is particularly important for dealing with problems of mean curvature flow type. In this paper we improve known finite volume schemes for solving 3D nonlinear diffusion (Corsaro et al., 2006) by speeding up the computations and keeping, or even improving, the precision and the second order accuracy. For large scale biological and medical applications that we have in

mind, such aspects are very important. We need precise, robust and mathematically and numerically reliable methods in any part of the image processing chain to be able to correctly interpret the biological data. For the semi-implicit finite volume schemes which we use for computations, the numerical analysis showing stability and consistency of discrete schemes for mean curvature flow models (Handlovičová et al., 2003; Handlovičová & Mikula, 2008) and convergence to continuous solutions and error estimates for the Perona-Malik type equations (Mikula & Ramarosy, 2001; Handlovičová & Krivá, 2005; Drblíková & Mikula, 2007a) was already done. That is a reason why we prefer (and present in this paper) such methods against e.g. semi-implicit additive operator splitting (AOS) methods (Weickert, 1999, 1998; Bruhn et al., 2004) for which no numerical analysis in case of nonlinear problems has been presented, although they represent fast and popular algorithms (the convergence of the AOS schemes to solution of the corresponding PDE is known only for the linear heat equation (Fischer & Modersitzki, 2002)). Moreover, since we need only a few successive-over-relaxation (SOR) iterations in the iterative linear algebra solver to get the solution at the new filtering step, the computational cost is comparable with additive operator splitting approach and we gain from theoretical analysis of the schemes. Our methods are also very simply parallelizable, by changing the SOR linear solver to the parallel Red-Black SOR method (Mikula & Sarti, 2007). The computational cost can then be significantly further reduced by straightforward parallel implementation.

In section 4, we carefully analyze the behavior of the methods when processing our 3D data sets. We first apply the methods using the same setting of parameters to learn their main properties and differences. This is achieved by quantitatively evaluating the filtering results using the mean Hausdorff distance of isosurfaces to a gold standard and checking the number of connected regions detected after the filtering. The optimal parameters are then chosen according to the best combination between the minimal mean Hausdorff distances observed for a large range of isosurfaces and the number of connected components detected in a region of interest. As preliminarily shown in Rizzi et. al (2007), this criterion is strongly related not only to the noise removal but also to the ability of edge preserving and enhancement. Another important criterion for embryogenesis image filtering is the ability to split artificially connected nuclei due to the physical constraints of LSM. We perform such analysis for the studied models and proposed schemes. The section is concluded by a comparison with two others well known nonlinear diffusion filtering models, the nonlinear tensor diffusion and the Beltrami flow.

The nonlinear diffusion filtering proves to be efficient and robust including a slight variation of chosen parameters. For the Perona-Malik, slowed and geodesic mean curvature flow models, the filtering significantly reduces the mean Hausdorff distance for a large range of isosurfaces. Such filtering always allows the extraction of the correct number of connected components of the

isosurface corresponding to the number of nuclei in the data subvolume. It turns out that the geodesic mean curvature flow has the best ability of splitting the artificially connected subregions. Taking into account all these aspects, the geodesic mean curvature flow (GMCF) becomes our preferable model for filtering 3D LSM images of early stages of embryogenesis.

2 Nonlinear diffusion filters

The nonlinear diffusion filters designed in this paper are based on numerical solution of nonlinear partial differential equations (PDEs) of a (degenerate) parabolic type (Alvarez et al., 1993). Such filters have been largely used for preprocessing the images prior further analysis (Sethian, 1999; Sapiro, 2001; Osher & Fedkiw, 2003). From the mathematical point of view, the processed input 3D image can be modeled by a real function $u^0(x)$, $u^0 : \Omega \to \mathbb{R}$, where $\Omega \subset \mathbb{R}^d, d = 3$ represents a spatial rectangular domain. Application of a PDE to a given image is also understood as its embedding in the so-called *scale space*. The Gaussian smoothing represents the *linear scale space*. In the case of nonlinear PDEs we speak about the *nonlinear scale space*. The axioms and fundamental properties of such embeddings have been summarized and studied by Alvarez et al. (1993). The image multiscale analysis associates to a given image $u^0(x)$ a family $u(t, x)$ of smoothed-simplified images depending on an abstract parameter $t \in [0, T]$, the *scale*. As has been proved in Alvarez et al. (1993), if such a family fulfills certain basic assumptions – pyramidal structure, regularity and local comparison principle – then $u(t, x)$, $u : [0, T] \times \Omega \to \mathbb{R}$, can be represented as the unique viscosity solution (in the sense of Crandall et al. (1992)) of a general second order (degenerate) parabolic partial differential equation. This theoretical result has also an important practical counterpart. The equations of (degenerate) parabolic type have a smoothing property, so they are a natural tool for filtering (simplifying the image) by removing spurious structures, e.g. noise. Moreover, the simplification should be "image oriented", e.g. it should recognize edges and not blur them, or it should be related to other geometrical characteristics like curvatures of image isosurfaces, bringing strong nonlinearity into the parabolic PDE. These properties make these methods interesting not only for important applications but also from the mathematical and numerical point of view. And, there are still many open questions how to push the-state-of-the-art models to the highest computational efficiency, mathematical reliability and applicability to various types of 3D+time image data sets.

The pioneering work of Perona & Malik (1987) modifying the linear heat equation to nonlinear diffusion preserving edge positions prompted a great deal of interest in the application and analysis of nonlinear diffusion equations for processing 2D and 3D images. The nonlinear PDE proposed by Catté et al. (1992) called *Perona-Malik* (PM) filter is widely used

$$u_t - \nabla.(g(|\nabla G_\sigma * u|)\nabla u) = 0. \tag{1}$$

From here and thereafter, $u(t,x)$ is an unknown function representing smoothed (filtered) image intensity defined in $Q_T \equiv [0,T] \times \Omega$. The equations are accompanied by zero Neumann boundary conditions and the initial condition

$$\partial u/\partial \nu = 0 \quad \text{on} \quad I \times \partial\Omega, \tag{2}$$

$$u(0,x) = u^0(x) \quad \text{in} \quad \Omega, \tag{3}$$

where ν is the unit normal vector to the boundary of Ω. We assume that

$$g : \mathbb{R}_0^+ \to \mathbb{R}^+ \text{ is a non increasing function,} \tag{4}$$

$$g(0) = 1, \quad \text{and we admit } g(s) \to 0 \text{ for } s \to \infty,$$

$$G_\sigma \in C^\infty(\mathbb{R}^d) \text{ is a smoothing kernel (e.g. the Gauss function),} \tag{5}$$

$$u^0 \in L_\infty(\Omega), \text{i.e., is a bounded function} \tag{6}$$

and convolution is defined by

$$\nabla G_\sigma * u = \int_{\mathbb{R}^d} \nabla G_\sigma(x-\xi)\tilde{u}(\xi)\, d\xi, \tag{7}$$

where $\tilde{u}$ is an extension of u to $\mathbb{R}^d$, e.g. a reflective periodic extension of the image (Catté et al., 1992).

The equation (1) represents a modification of the original Perona-Malik model (Perona & Malik, 1987; Nitzberg & Shiota, 1992; Kichenassamy, 1997)

$$u_t - \nabla.(g(|\nabla u|)\nabla u) = 0, \tag{8}$$

called also *anisotropic diffusion* in the computer vision community. Perona and Malik introduced (8) in the context of edge enhancement. From a mathematical point of view, for practical choices of g (e.g. $g(s) = 1/(1+Ks^2)$, $g(s) = \exp(-Ks^2), K > 0$), the original Perona-Malik equation can behave locally like the backward heat equation. It is, in general, an ill-posed problem suffering from non-uniqueness and its solvability is a difficult problem (Kichenassamy, 1997). One way to overcome this theoretical disadvantage has been proposed by Catté et al. (1992). They introduced the convolution with

the Gaussian kernel G_σ into the decision process for the value of the diffusion coefficient. Since convolution with the Gaussian is equivalent to linear diffusion, their model combines ideas of linear and nonlinear scale space equations. Such a slight modification made it possible to prove the existence and uniqueness of solutions for the modified equation, and to keep the practical advantages of the original formulation. Moreover, usage of the *Gaussian gradient* $\nabla G_\sigma * u$ combines the theoretical and implementation aspects of the model. The convolution (with prescribed σ) represents a unique way to compute gradients of a piecewise constant image. It also bounds (depending on σ) the gradient of the solution as the input of the function g in the continuous model – which corresponds to the situation in numerical implementations where gradients evaluated on a discrete grid are finite. Also, the local edge enhancement is more understandable in the presence of noise when using G_σ regularization.

2.2 The curvature-driven nonlinear diffusion filtering equations

In rather general situations, edges correspond to specific level lines (in 2D images) and level surfaces (in 3D images) of the image intensity function (Cao, 2004). Then the smoothing corresponds to their properly designed evolution. The motion of isosurfaces in the normal direction depending on curvature, namely the so-called *mean curvature flow* (MCF) equation in the level set formulation

$$u_t = |\nabla u| \nabla . \left(\nabla u / |\nabla u| \right) , \tag{9}$$

is a natural choice for such *geometrical* filtering, and it is known as *curvature filter* in computer vision community. Unlike the Lagrangian approaches to curve and surface evolution, the level set formulation brings the smoothing of all level sets at once. The contrast invariance of (9) has a large significance in the axiomatic theory of the image processing and computer vision (Alvarez et al., 1993).

A useful generalization of (9) in the context of image filtering was suggested by Alvarez et al. (1992)

$$u_t = g(|\nabla G_\sigma * u|) |\nabla u| \nabla . \left(\nabla u / |\nabla u| \right) . \tag{10}$$

Equation (10) can be used either for uniform intrinsic isosurface smoothing (provided $g \equiv 1$), or for edge-preserving smoothing similarly as the equation (1). The Perona-Malik function $g(s)$ depending on $|\nabla G_\sigma * u|$ is used to strongly slow down the mean curvature driven motion of isosurfaces which represent edges, and regions outside edges are smoothed by the uniform mean curvature flow. We call this model the *slowed mean curvature flow* (SMCF) filter.

The level set equation (9) can be generalized also in the following sense (Chen et al., 2000)

$$u_t = |\nabla u| \nabla . \left(g(|\nabla G_\sigma * u|) \nabla u / |\nabla u| \right) \tag{11}$$

which we call the *geodesic mean curvature flow* (GMCF) filter. If $g \equiv g(|\nabla G_\sigma * u|)$ is replaced by $g(|\nabla G_\sigma * u^0|)$, the equation is used in image segmentation as originally proposed by Caselles et al (1997a,b) and Kichenassamy et al. (1996). It has been also used for filtering 3D confocal images in Sarti et al. (2000). Although the equations (10) and (11) look similar, their structure is different. In contrast to (10), in (11) the weighting term $g(|\nabla G_\sigma * u|)$ is inside a divergence operator which brings new important advective phenomenon into the model. One can see (11) rewritten into the advection-diffusion form

$$u_t = g|\nabla u| \nabla . \left(\nabla u / |\nabla u| \right) + \nabla g . \nabla u. \tag{12}$$

The advective term given by the vector field $-\nabla g$ drives all level sets to the image edges and brings their enhancement. It is combined with smoothing outside the edge regions. One can also see an analogy with the Perona-Malik model that can be written as

$$u_t = g \Delta u + \nabla g . \nabla u \tag{13}$$

with the Laplacian linear diffusion term in (13) replaced by the mean curvature flow of level sets in (12). The model (10) can be seen as just a diffusive part of the model (12), without the advection of level sets.

All level set equations mentioned above, (9), (10), (11), are regularized by the Evans-Spruck ε-regularization (Evans & Spruck, 1992)

$$|\nabla u| \approx |\nabla u|_\varepsilon = \sqrt{\varepsilon^2 + |\nabla u|^2}. \tag{14}$$

E.g. the ε-regularization of (11) is given by

$$u_t = \sqrt{\varepsilon^2 + |\nabla u|^2} \nabla . \left(g(|\nabla G_\sigma * u|) \nabla u / \sqrt{\varepsilon^2 + |\nabla u|^2} \right). \tag{15}$$

In all cases the parameter ε, $0 < \varepsilon \leq 1$ shifts the models from the (slowed, geodesic) mean curvature flow of graph ($\varepsilon = 1$) to the mean curvature flow of level sets ($\varepsilon = 0$). All curvature level set equations are accompanied by the boundary and initial conditions (2)–(3) and the assumptions (4)–(6) are fulfilled.

3 Discrete filtering methods based on discretization of nonlinear PDEs

Since 3D images are given on a discrete grid (voxel structure) and we are interested in subsequent time steps leading to optimal filtering result, we discretized the partial differential equations in space and time to get a scheme implemented on a (parallel) computer. In order to fulfill unconditional stability constraint which naturally prevents the solution from spurious oscillations, we used semi-implicit time discretizations (Kačur & Mikula, 1995), and, employing the divergence structure of the equations, we used the finite volume method for spatial discretization, see e.g (Mikula & Ramarosy, 2001; Krivá & Mikula, 2002; Handlovičová et al., 2003, 2002; Mikula et al., 2005) for 2D image filtering and segmentation by the Perona-Malik and mean curvature flow type equations. 3D semi-implicit finite volume methods for the Perona-Malik-type problems were presented in (Sarti et al., 1999; Krivá & Mikula, 2001; Sarti et al., 2002). The first 3D computational method for the mean curvature flow type problems in level set formulation based on the finite volume discretization was developed in Corsaro et al. (2006). The scheme can be derived using the so-called diamond cell strategy applied to 3D problems where the approximation of solution gradient, which is needed in mean curvature or Perona-Malik type problems, is consistently defined on every voxel side, see e.g. Coudiere et al. (1999); Drblíková & Mikula (2007a,b), by the construction of a covolume in the form of a diamond. The scheme from Corsaro et al. (2006) is obtained by further splitting such 3D diamond cell to four tetrahedra and then linear representation of solution is used to approximate gradients on the voxel side. In this paper, we introduce a new 3D finite volume scheme given by a proper reduction of stencil of the full diamond cell method, cf. also Mikula & Remešíková (2009). This new scheme is more precise and faster (because it uses smaller stencil for evaluation of nonlinear diffusion coefficients in every filtering step) than the one presented in Corsaro et al. (2006) and it has the same unconditional stability property as the previous one. By those observations, it seems optimal for our 3D nonlinear filtering problems.

3.1 Semi-implicit time discretizations

Choosing $N \in \mathbb{N}$ we obtain the length of the uniform discrete time step $\tau = T/N$. We replace the time derivative in the equations by the backward difference and nonlinear terms in equations are considered at the previous time step while linear terms are taken at the current time step. In such way we get the semi-implicit time discretizations.

3.1.1 Semi-implicit scheme for the regularized Perona-Malik equation (1):

Let $N \in \mathbb{N}$, $\tau = T/N$ and $\sigma > 0$ be fixed numbers, and let u^0 be given by (3). For every $n = 1, \ldots, N$, we look for a function u^n which satisfies the equation

$$(u^n - u^{n-1})/\tau - \nabla.(g(|\nabla u_\sigma^{n-1}|)\nabla u^n) = 0 \tag{16}$$

where we use notation

$$u_\sigma^{n-1} = G_\sigma * u^{n-1} \tag{17}$$

In discretization of the equation (9) we employ its variational structure. First we move the term which is in front of the divergence to the time derivative, and then we write semi-implicit discretization as follows.

3.1.2 Semi-implicit scheme for the mean curvature flow equation (9):

Let $N \in \mathbb{N}$, $\tau = T/N$ and $\sigma > 0$ be fixed numbers, and let u^0 be given by (3). For every $n = 1, \ldots, N$, we look for a function u^n which satisfies the equation

$$1/|\nabla u^{n-1}|\ (u^n - u^{n-1})/\tau - \nabla.\left(\nabla u^n/|\nabla u^{n-1}|\right) = 0. \tag{18}$$

Similarly we get the semi-implicit schemes for the next two models.

3.1.3 Semi-implicit scheme for the slowed mean curvature flow equation (10):

Let $N \in \mathbb{N}$, $\tau = T/N$ and $\sigma > 0$ be fixed numbers, and let u^0 be given by (3). For every $n = 1, \ldots, N$, we look for a function u^n which satisfies the equation

$$1/(g(|\nabla u_\sigma^{n-1}|)|\nabla u^{n-1}|)\,(u^n - u^{n-1})/\tau - \nabla.\left(\nabla u^n/|\nabla u^{n-1}|\right) = 0. \tag{19}$$

3.1.4 Semi-implicit scheme for the geodesic mean curvature flow equation (11):

Let $N \in \mathbb{N}$, $\tau = T/N$ and $\sigma > 0$ be fixed numbers, and let u^0 be given by (3). For every $n = 1, \ldots, N$, we look for a function u^n which satisfies the equation

$$1/|\nabla u^{n-1}|\,(u^n - u^{n-1})/\tau - \nabla.\left(g(|\nabla u_\sigma^{n-1}|)\,\nabla u^n/|\nabla u^{n-1}|\right) = 0. \tag{20}$$

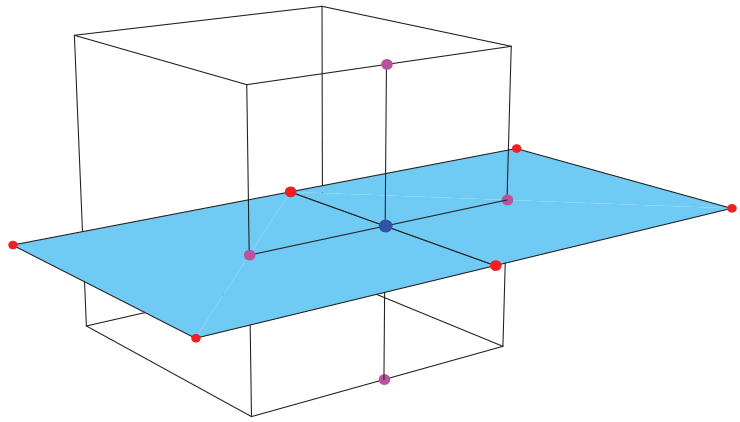

Fig. 2. Voxel (box by black lines), point x_{ijk}^{100} (blue) on the "east" side where the gradient is approximated, voxel centers (red points) and points which are used for approximation of gradient in tangential direction (violet).

3.2 Finite volume space discretizations

In order to provide spatial discretizations we employ the so-called finite volume method. We identify the finite volume mesh $\mathcal{T}_h$ with the voxels of 3D image and denote each finite volume by V_{ijk}, $i = 1, \ldots, N_1$, $j = 1, \ldots, N_2$, $k = 1, \ldots, N_3$. For each $V_{ijk} \in \mathcal{T}_h$ let N_{ijk} denote the set of all neighboring (west, east, south, north, bottom and top) volumes $V_{i+p,j+q,k+r}$, $p, q, r \in \{-1, 0, 1\}$, $|p| + |q| + |r| = 1$. Let $m(V_{ijk})$ denote volume of V_{ijk}. The edge connecting center of V_{ijk} and center of its neighbor $V_{i+p,j+q,k+r} \in N_{ijk}$ is denoted by σ_{ijk}^{pqr} and its length by h_{ijk}^{pqr}. Since our finite volume grid is regular rectangular we will use also shorter notations h_1 for $h_{ijk}^{p00}, p \in \{-1, 1\}$, h_2 for $h_{ijk}^{0q0}, q \in \{-1, 1\}$ and h_3 for h_{ijk}^{00r}, $r \in \{-1, 1\}$ representing sizes of finite volumes in x_1, x_2, x_3 direction, respectively. The planar sides of finite volume V_{ijk} are denoted by e_{ijk}^{pqr} with area $m(e_{ijk}^{pqr})$. The edge σ_{ijk}^{pqr} crosses the side e_{ijk}^{pqr} in the point x_{ijk}^{pqr}, see Figure 2.

We present the idea of finite volume discretization for equation (11) which is the most complex concerning differential terms. As it is standard in finite volume methods (LeVeque, 2002; Eymard et al., 2000) we integrate (20) over every finite volume V_{ijk}. We get

$$\int_{V_{ijk}} 1/|\nabla u^{n-1}| \, (u^n - u^{n-1})/\tau dx = \int_{V_{ijk}} \nabla . \left(g(|\nabla u_\sigma^{n-1}|) \, \nabla u^n / |\nabla u^{n-1}| \right) dx. \quad (21)$$

Using divergence theorem for the right hand side of (21) we get

$$\int\limits_{V_{ijk}} \nabla.\left(g(|\nabla u_\sigma^{n-1}|)\,\nabla u^n/|\nabla u^{n-1}|\right)dx = \int\limits_{\partial V_{ijk}} g(|\nabla u_\sigma^{n-1}|)/|\nabla u^{n-1}\,|\partial u^n/\partial\nu ds$$
$$= \sum_{|p|+|q|+|r|=1} \int\limits_{e_{ijk}^{pqr}} g(|\nabla u_\sigma^{n-1}|)/|\nabla u^{n-1}|\,\partial u^n/\partial\nu ds$$

where ν denotes the outer unit normal to the finite volume. We have got the integral formulation of (20)

$$\int\limits_{V_{ijk}} 1/|\nabla u^{n-1}|(u^n - u^{n-1})/\tau dx =$$
$$\sum_{|p|+|q|+|r|=1} \int\limits_{e_{ijk}^{pqr}} g(|\nabla u_\sigma^{n-1}|)/|\nabla u^{n-1}|\partial u^n/\partial\nu ds. \quad (22)$$

Taking into account a natural connection between image processing applications and finite volume methods, namely that fully discrete approximate solution u_{ijk}^n inside finite volume at time level n represents an average value of image intensity inside the voxel V_{ijk} we can naturally express the left hand side as

$$\int\limits_{V_{ijk}} 1/|\nabla u^{n-1}|(u^n - u^{n-1})/\tau dx \approx m(V_{ijk})/\overline{Q}_{ijk}^{n-1}\,(u_{ijk}^n - u_{ijk}^{n-1})/\tau \quad (23)$$

where $\overline{Q}_{ijk}^{n-1}$ is an average modulus of gradient in V_{ijk}. This average will be computed using values of the gradients on sides e_{ijk}^{pqr} of the finite volume, which must be approximated on the right hand of (22) as well. On the right hand side of (22), the normal derivative is naturally expressed by the finite difference of neighboring voxel values divided by the distance between voxel centers. To approximate the modulus of gradients on voxel sides, we use following definitions for $p, q, r \in \{-1, 0, 1\}, |p| + |q| + |r| = 1$,

$$\nabla^{p00}u_{ijk}^n = (p(u_{i+p,j,k}^n - u_{ijk}^n)/h_1, (u_{ijk}^{p10} - u_{ijk}^{p,-1,0})/h_2, (u_{ijk}^{p01} - u_{ijk}^{p,0,-1})/h_3), (24)$$
$$\nabla^{0q0}u_{ijk}^n = ((u_{ijk}^{1q0} - u_{ijk}^{-1,q,0})/h_1, q(u_{i,j+q,k}^n - u_{ijk}^n)/h_2, (u_{ijk}^{0q1} - u_{ijk}^{0,q,-1})/h_3), (25)$$
$$\nabla^{00r}u_{ijk}^n = ((u_{ijk}^{10r} - u_{ijk}^{-1,0,r})/h_1, (u_{ijk}^{01r} - u_{ijk}^{0,-1,r})/h_2, r(u_{i,j,k+r}^n - u_{ijk}^n)/h_3), (26)$$

where

$$u_{ijk}^{pq0} = 1/4(u_{ijk}^n + u_{i+p,j,k}^n + u_{i,j+q,k}^n + u_{i+p,j+q,k}^n), \quad (27)$$
$$u_{ijk}^{p0r} = 1/4(u_{ijk}^n + u_{i+p,j,k}^n + u_{i,j,k+r}^n + u_{i+p,j,k+r}^n), \quad (28)$$
$$u_{ijk}^{0qr} = 1/4(u_{ijk}^n + u_{i,j+q,k}^n + u_{i,j,k+r}^n + u_{i,j+q,k+r}^n) \quad (29)$$

represent the approximate values of u in the centers of voxel edges (violet points in Figure 2) taken as an average of neighboring voxel values (red points in Figure 2) in corresponding cutting planes (blue planes in Figure 2). It should be noted that to avoid any confusion, in the above formulas and below we use commas in superscripts and subscripts only when some of the p, q, r is negative in superscript, or if there is a summation of indices in subscripts.

The formulas (24)-(26) can be understood as an approximation of the gradient in the point x_{ijk}^{pqr} (blue point in Figure 2) which is a barycenter of e_{ijk}^{pqr} .

Now we define

$$Q_{ijk}^{pqr;n-1} = \sqrt{\varepsilon^2 + |\nabla^{pqr} u_{ijk}^{n-1}|^2}, \quad \overline{Q}_{ijk}^{n-1} = \sqrt{\varepsilon^2 + 1/6 \sum_{|p|+|q|+|r|=1} |\nabla^{pqr} u_{ijk}^{n-1}|^2}$$

as a regularized absolute value of the gradient on voxel sides, and, the regularized averaged gradient inside the finite volume, respectively, computed by the solution known from the previous time step $n-1$. Similarly we compute the Perona-Malik terms, where the function g is applied to the gradient of convolved solution u_σ on voxel sides (or inside the voxel in case of SMCF filter), namely we define

$$g_{ijk}^{pqr;n-1} = g(|\nabla^{pqr} u_{\sigma;ijk}^{n-1}|)\,, \quad g_{ijk}^{n-1} = g\left(1/6 \sum_{|p|+|q|+|r|=1} |\nabla^{pqr} u_{\sigma;ijk}^{n-1}|\right).$$

Let us note that the convolution is realized solving numerically the linear diffusion equation with the initial condition given by u^{n-1} using one implicit time step corresponding to the variance σ. Combining all the above considerations we end up with the following approximation

$$\begin{aligned} &\sum_{|p|+|q|+|r|=1} \int_{e_{ijk}^{pqr}} g(|\nabla u_\sigma^{n-1}|)/|\nabla u^{n-1}| \partial u^n/\partial \nu ds \\ &\quad \approx \sum_{|p|+|q|+|r|=1} m(e_{ijk}^{pqr}) g_{ijk}^{pqr;n-1}/Q_{ijk}^{pqr;n-1}\ (u_{i+p,j+q,k+r}^n - u_{ijk}^n)/h_{ijk}^{pqr} \quad (30) \end{aligned}$$

If we put together the right hand sides of (23) and (30) and consider zero Neumann boundary conditions, we can write the following linear system of equations which has to be solved at every discrete time step n, $n = 1, \ldots, N$, where N is a total number of filtering steps:

$$\begin{aligned} &\sum_{|p|+|q|+|r|\le 1} A_{ijk}^{pqr}\ \ u_{i+p,j+q,k+r}^n = u_{ijk}^{n-1}, \\ &\qquad\qquad i = 1, \ldots, N_1,\ j = 1, \ldots, N_2,\ k = 1, \ldots, N_3. \quad (31) \end{aligned}$$

Then the **discrete GMCF filter** is given by solving the system (31) for $n = 1, \ldots, N$ with coefficients defined as follows

$$\begin{aligned} A_{ijk}^{pqr} &= -(\tau\ m(e_{ijk}^{pqr})\ g_{ijk}^{pqr;n-1}\ \overline{Q}_{ijk}^{n-1})/(m(V_{ijk})\ Q_{ijk}^{pqr;n-1}\ h_{ijk}^{pqr}), \\ &\quad |p|+|q|+|r| = 1\,, \quad x_{ijk}^{pqr} \notin \partial\Omega \\ A_{ijk}^{000} &= 1 + \sum_{|p|+|q|+|r|=1} -A_{ijk}^{pqr}\,, \quad A_{ijk}^{pqr} = 0\,, \quad \text{otherwise.} \end{aligned} \tag{32}$$

Similarly, the **discrete MCF filter** is given by (31) with coefficients

$$\begin{aligned} A_{ijk}^{pqr} &= -(\tau\ m(e_{ijk}^{pqr})\ \overline{Q}_{ijk}^{n-1})/(m(V_{ijk})\ Q_{ijk}^{pqr;n-1}\ h_{ijk}^{pqr}), \\ &\quad |p|+|q|+|r| = 1\,, \quad x_{ijk}^{pqr} \notin \partial\Omega \\ A_{ijk}^{000} &= 1 + \sum_{|p|+|q|+|r|=1} -A_{ijk}^{pqr}\,, \quad A_{ijk}^{pqr} = 0\,, \quad \text{otherwise.} \end{aligned} \tag{33}$$

The **discrete SMCF filter** is given by (31) with coefficients

$$\begin{aligned} A_{ijk}^{pqr} &= -(\tau\ m(e_{ijk}^{pqr})\ g_{ijk}^{n-1}\ \overline{Q}_{ijk}^{n-1})/(m(V_{ijk})\ Q_{ijk}^{pqr;n-1}\ h_{ijk}^{pqr}), \\ &\quad |p|+|q|+|r| = 1\,, \quad x_{ijk}^{pqr} \notin \partial\Omega \\ A_{ijk}^{000} &= 1 + \sum_{|p|+|q|+|r|=1} -A_{ijk}^{pqr}\,, \quad A_{ijk}^{pqr} = 0\,, \quad \text{otherwise} \end{aligned} \tag{34}$$

and the **discrete PM filter** is given by (31) with coefficients

$$\begin{aligned} A_{ijk}^{pqr} &= -(\tau\ m(e_{ijk}^{pqr})\ g_{ijk}^{pqr;n-1})/(m(V_{ijk})\ h_{ijk}^{pqr}), \\ &\quad |p|+|q|+|r| = 1\,, \quad x_{ijk}^{pqr} \notin \partial\Omega \\ A_{ijk}^{000} &= 1 + \sum_{|p|+|q|+|r|=1} -A_{ijk}^{pqr}\,, \quad A_{ijk}^{pqr} = 0\,, \quad \text{otherwise.} \end{aligned} \tag{35}$$

Since the structure of the linear system for all methods is the same and it is suitable for using iterative solvers, we use the so-called successive over relaxation (SOR) method, which is a modification of the Gauss-Seidel method to speed up its convergence, and can be written as follows

$$Y = \left(u_{ijk}^{n-1} - \sum_{\substack{|p|+|q|+|r|=1 \\ p,q,r\in\{-1,0\}}} A_{ijk}^{pqr} u_{i+p,j+q,k+r}^{n\ (l)} - \sum_{\substack{|p|+|q|+|r|=1 \\ p,q,r\in\{0,1\}}} A_{ijk}^{pqr} u_{i+p,j+q,k+r}^{n\ (l-1)} \right) / A_{ijk}^{000}$$

$$u_{ijk}^{n\ (l)} = u_{ijk}^{n\ (l-1)} + \omega(Y - u_{ijk}^{n\ (l-1)})$$

$$i = 1, \ldots, N_1,\ j = 1, \ldots, N_2, k = 1, \ldots, N_3,\ l = 1, 2, ...,\quad u_{ijk}^{n\ (0)} = u_{ijk}^{n-1},$$

with (l) representing the iteration number and with a relaxation parameter

$\omega \in (0,2)$. In practice we use ω around 1.5 and stop the iterations when relative residual drops bellow a prescribed tolerance.

For all the models and semi-implicit finite volume schemes we can state following existence and unconditional stability results.

Theorem. *In every step $n = 1, \ldots, N$, there exists unique solution for all the schemes (32)-(35) for any choice of time step $\tau > 0$ and regularization parameter $\varepsilon > 0$. The unique solution can be found using Gauss-Seidel (SOR) iterative method. Moreover, for any $\tau > 0$, $\varepsilon > 0$ the following L_∞ stability estimate (minimum-maximum principle) holds*

$$\min_{ijk} \; u^0_{ijk} \leq \min_{ijk} \; u^n_{ijk} \leq \max_{ijk} \; u^n_{ijk} \leq \max_{ijk} \; u^0_{ijk}, \quad 1 \leq n \leq N. \tag{36}$$

Proof. All the matrices of the linear systems are strictly diagonally dominant and, thus, invertible, so we can assert that the solution always exists and is unique. In such case, it is also guaranteed that the Gauss-Seidel (SOR) iterative method converges to this solution. The linear system (31) can be written in the form

$$u^n_{ijk} + \sum_{|p|+|q|+|r|=1} A^{pqr}_{ijk}(u^n_{i+p,j+q,k+r} - u^n_{ijk}) = u^{n-1}_{ijk} \tag{37}$$

and let $\max_{ijk} u^n_{ijk}$ be achieved in the volume V_{ijk}. Due to nonpositivity of all terms A^{pqr}_{ijk} and nonpositivity of the difference terms inside the summation in (37) we have that the entire sum on the left hand side is nonnegative and thus $u^n_{ijk} \leq u^{n-1}_{ijk}$ which is clearly less or equal to maximum at the previous time level. Similarly we can get the relation for minimum and, recursively, we have that all solution values computed by the schemes are inside the range $[\min_{ijk} \; u^0_{ijk}, \max_{ijk} \; u^0_{ijk}]$.

In order to complete the discussion on properties of our schemes we made a computational comparison with the known exact solution of the mean curvature flow problem (9) which is given by the function , cf. (Oberman, 2004),

$$u(x,y,z,t) = (x^2 + y^2 + z^2 - 1)/4 + t. \tag{38}$$

In this test, we considered the Dirichlet boundary conditions given by the exact solution. We solved the problem in the spatial domain $\Omega = [-1.25, 1.25]^3$ and in the time interval $T = 0.16$. We have taken subsequent grid refinement with $M = n^3$ finite volumes, $n = 20, 40, 80, 160$, and the voxel size is $h = 2.5/n$. As usually done in testing numerical solutions of parabolic problems, the time step τ is chosen proportionally to h^2. The parameter $\varepsilon = 10^{-6}$, and we measure the errors in $L_\infty((0,T), L_2(\Omega))$-norm, cf. (Deckelnick & Dziuk, 2000). The

Table 1
Errors in $L_\infty((0,T), L_2(\Omega))$-norm, EOC comparing numerical and exact solutions (38) and CPU time for one time step.

h	τ	method from Corsaro et al.	method (33)	EOC	CPU
0.125	0.016	5.23e-3	1.08e-3		0.012
0.0625	0.004	1.29e-3	2.66e-4	2.02	0.109
0.03125	0.001	3.23e-4	6.65e-5	2.00	0.8
0.015625	0.00025	8.05e-5	1.64e-5	2.02	6.7

parameter $\omega = 1.5$ in the SOR solver. A powerful method for checking the convergence of the method to the solution of the continuous problem is the study of the so called *experimental order of convergence* (EOC). It is standard to provide such a study in order to show reliability of the numerical method in engineering simulations. The basic idea is the following. Let us assume that the error of the scheme in some norm is proportional to some power of the grid size, i.e. $Error(h) = Ch^\alpha$, with a constant C. Then halving the grid size we have $Error(h/2) = C(h/2)^\alpha$ from where we can simply extract

$$\alpha = \log_2(Error(h)/Error(h/2)). \tag{39}$$

Such α gives EOC of the method and can be determined by comparing numerical solutions and exact solution on subsequently refined grids.

In Table 1 we report in the 3rd column the errors given by the state-of-the-art co-volume method from Corsaro et al. (2006) applied to (9) , in the 4th column our new method presented in this paper, in the 5th column EOC of our new method and in the 6th column the CPU needed for solving one time step of the method. The resolution of the grid given by h and time step τ are given in the 1st and 2nd columns of the Table. The most important observation is that the method is experimentally second order accurate, i.e. $\alpha = 2$. Our new method gives approximately 5 times smaller error than the method from Corsaro et al. (2006). Concerning computational efficiency, solving nonlinear diffusion problems, a relatively large portion of CPU time at every time step is related to the evaluation of diffusion coefficients on voxel sides. On the fine grid with $n = 160$, cf. Table 1, this step takes $1.49s$ for our new method while it last $3.53s$ for the method from Corsaro et al. (2006). Since the solution of the linear system takes approximately same time for both methods, this difference represents a speed-up of the new method. We also get a nice scaling, approximately by 8, of the CPU time in one time step. Since the number of unknowns is increasing by this factor 8 in every refinement step, the computational complexity of the method is growing linearly. Since for filtering we always use just a few discrete time steps, our method is of order $O(M)$ where M is the number of voxels.

4 Discussion on computational results

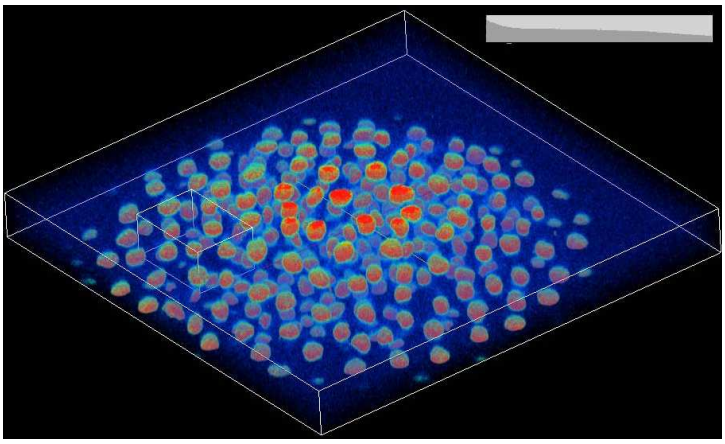

Fig. 3. The original noisy data in volume rendering representation. The subvolume selected to construct the gold standard is shown in the small white bounding box. This subvolume consists of 71x100x28 voxels. On the top-right is the image histogram, the gray bar below the histogram shows the range of values between 25 and 30. For an isosurface representation of various ROI in this data set we refer also to Figures 11-12.

In this section we show and discuss the results obtained applying the methods described above to 3D+time images of Danio Rerio embryo nuclei. The data has been acquired using a Confocal Microscope Leica SP2 AOBS (Megason & Fraser, 2003). The whole sequence consists in 49 time steps, with one 3D image completed every 5 minutes and has size 512x512x30 voxels. The dimension of each voxel is 0.58x0.58x1.05 μ^3. The data was acquired for four hours (25°C under the microscope), starting at 3,5 hours post fertilization (development at 28°C) (Kimmel et al., 1995). In the entire period of development, the whole embryo looks like a sphere with a diameter of 740 μ. The images have a physical dimension of 300 x 300 x 31 μ^3 and cover only the top part of the embryo, as shown in Figure 1. The data should be preprocessed with appropriate filtering procedures for further image analysis in order to reconstruct the cell lineage tree through the extraction of the approximate cell center positions (Drblíková et al., 2007; Frolkovič et al., 2007; Melani al., 2007), cell segmentation (Drblíková et al., 2007; Frolkovič et al., 2007; Zanella et al., 2007, 2009), velocity field extraction and cell tracking (Melani al., 2007). The filtering step should remove the noise and smooth small variations in image intensity while maintaining a good definition of image features and keeping useful features such as edges. The performances of our filtering methods are evaluated by visual inspection and quantitative analysis as well as by their computational cost. The quantitative analysis consists in calculating the mean Hausdorff distance between a gold standard, obtained by manual segmentation, and isosurfaces of original and filtered data chosen around the nuclei boundaries. As previously introduced in Rizzi et. al (2007), this method allows to evaluate the

ability of smoothing and sharpening of the filtering models. We also compare the number of nuclei found in the manually segmented region of interest with the connected components of the isosurface detected in the same ROI before and after the filtering. Our analysis continues by quantifying the ability of tested methods to divide the very close nuclei, artificially connected because of the acquisition error intrinsically linked to physics of the image acquisition system. In this section, we first introduce the gold standard and the mean Hausdorff distance. We then discuss the behavior of all the methods, first using the same values of parameters adopting the multiscale analysis point of view. The mean Hausdorff distance information, combined with the analysis of connected components, is then used to choose optimal values of parameters for the methods. The related results are afterwards discussed and compared and even improved by a splitting analysis. The section ends with a comparison with the nonlinear tensor diffusion and the Beltrami flow methods.

4.1 The mean Hausdorff distance and the gold standard

Let $A = \{a_1, \ldots, a_p\}$ and $B = \{b_1, \ldots, b_q\}$ denote two finite point sets, the *mean Hausdorff distance* is defined as (Zhang et al., 2005)

$$MHD(A, B) = \max\left(mhd(A, B), mhd(B, A)\right)$$

where

$$mhd(A, B) = 1/p \sum_{i=1}^{p} \min_{b \in B} \|a_i - b\|$$

is called *mean directed Hausdorff distance* and $\|\cdot\|$ is some underlying norm (usually Euclidean) on the points of sets A, B. The $mhd(B, A)$ is defined similarly. The mean Hausdorff distance is widely used to measure the mismatch between two point sets, see e.g. (Huttenlocher et al., 1993; Zhang et al., 2005), usually to perform an image matching. In our case the sets A and B are given by discrete points that form the surface of the gold standard and an isosurface either in original or in filtered volume.

To quantitatively compare the models, paying particular attention to the ability of the methods to preserve (or even enhance) the edges of objects in 3D images, we selected a region of interest in the first unfiltered frame of the time sequence and we manually segmented a gold standard, as shown in Figures 3 and 4. We then calculated the mean Hausdorff distance between the manually segmented nuclei surfaces in the gold standard and the corresponding nuclei isosurfaces in the original and filtered data, respectively. Observing the image histogram and using visual inspection we estimated the levels of intensity between 25 and 30 as the closest to the "real" boundaries of nuclei. In order to evaluate the behavior of the denoising methods in this interval of

gray levels, we selected isosurface levels around these values, from 15 to 45 with step 5. For every such isosurface either in original or in filtered data, we selected a nucleus surface in the gold standard, found the corresponding nucleus surface, and calculated their mean Hausdorff distance. At the end we averaged the mean Hausdorff distances over all nuclei in the subvolume. To check the matching between the gold standard and raw or filtered data we visualized their overlapping within their bounding boxes, see Figure 5. In order to take into account not only the mean Hausdorff distance which is evaluated just for one connected component of isosurface level set (the largest one), we also counted the total number of regions (connected components of isosurface)

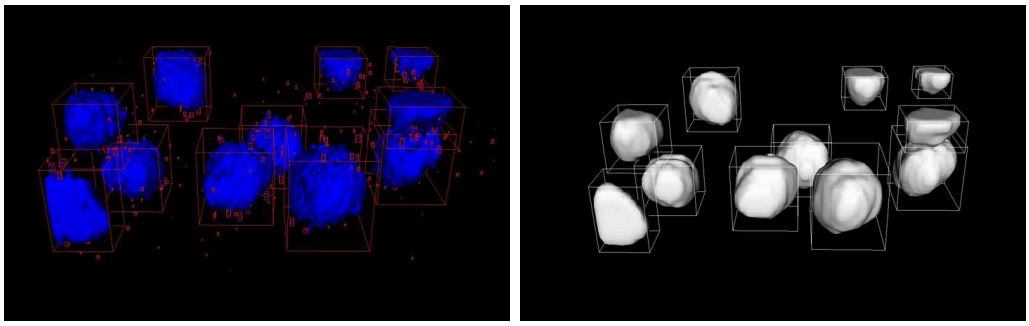

(a) (b)

Fig. 4. Comparison between the selected ROI of original data and its manual segmentation, chosen as gols standard. (a) Isosurface 25 in the ROI of original data depicted in blue. A red bounding box surrounds every object (nuclei and noise) inside the region. (b) Gold standard, represented in white. Every nucleus is surrounded by a white bounding box

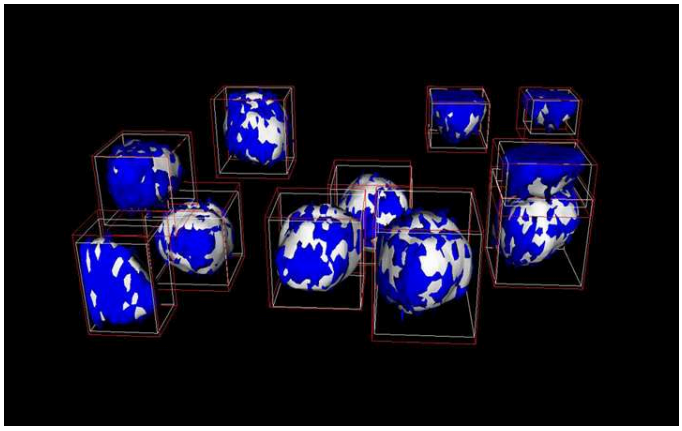

Fig. 5. Comparison between the selected ROI of original data and the gold standard. The plot of 11 nuclei of the gold standard (white) overlaps the corresponding component of isosurface 25 in the original data set (blue), for which we compute the mean Hausdorff distances. Each nucleus, both in original data and in the gold standard, is sourrounded by its bounding box (red and white, respectively). Small regions due to noise are not included in the computation of the mean Hausdorff distance and are not represented.

found in the subvolume and compared this number with the number of nuclei in the gold standard. This enabled us to evaluate the ability of our methods of removing the spurious, noisy structures from the image.

4.2 Comparison of the filtering models using the same settings of parameters

To see the basic differences between the models applied to our data set, we let the algorithms run for the same time with the same setting of parameters. We use the function $g(s) = 1/(1 + Ks^2)$, $K = 1$, $h_{ijk}^{pqr} = h = 0.01$, $\tau = 0.0001$ (i.e. we use relation $\tau \approx h^2$ which is natural for numerical solution to parabolic equations), $\sigma = 0.0001$ (i.e. the amount of presmoothing due to convolution is proportional to time step) and we check the solutions after 5, 10 and 15 time steps. Let us note that $m(e_{ijk}^{pqr}) = h^2$ and $m(V_{ijk}^{pqr}) = h^3$ in the scheme coefficients.

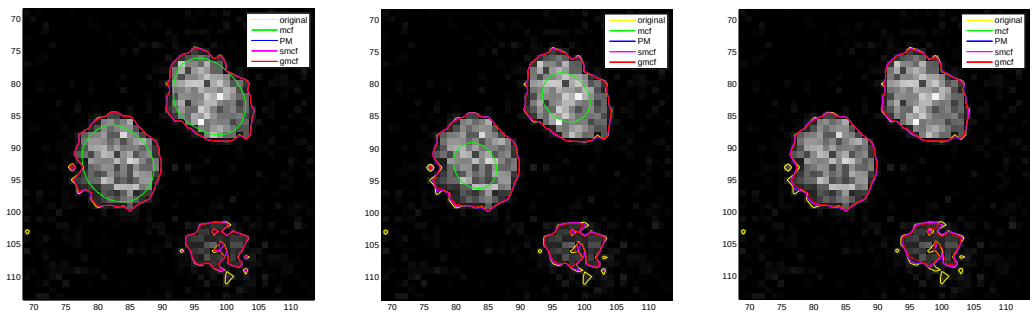

(a) (b) (c)

Fig. 6. A 2D cut of original data and the cut of isosurface of value 28 of original and filtered data using same setting of filtering parameters ($K = 1, \sigma = 0.0001, \tau = 0.0001$) after 5 (a), 10 (b) and 15 (c) time steps.

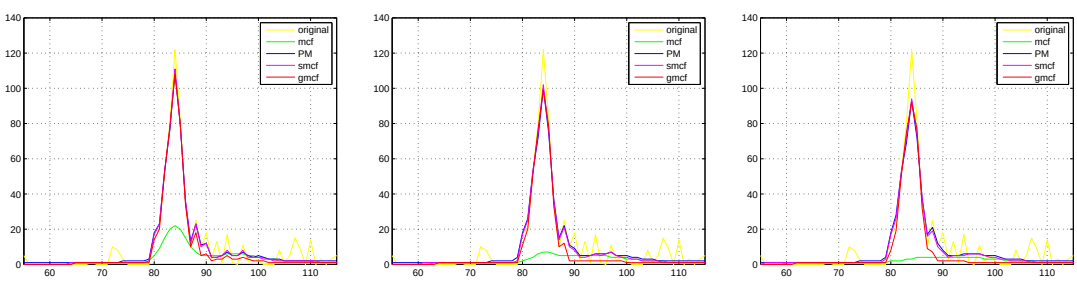

(a) (b) (c)

Fig. 7. Graphs of the original and filtered image intensities in a neighborhood of one of the nuclei from Figure 6 after 5 (a), 10 (b) and 15 (c) time steps.

Figure 6 shows three nuclei chosen to compare the behavior of the models. A cut of original data is superimposed on the cut of isosurface 28 of the original

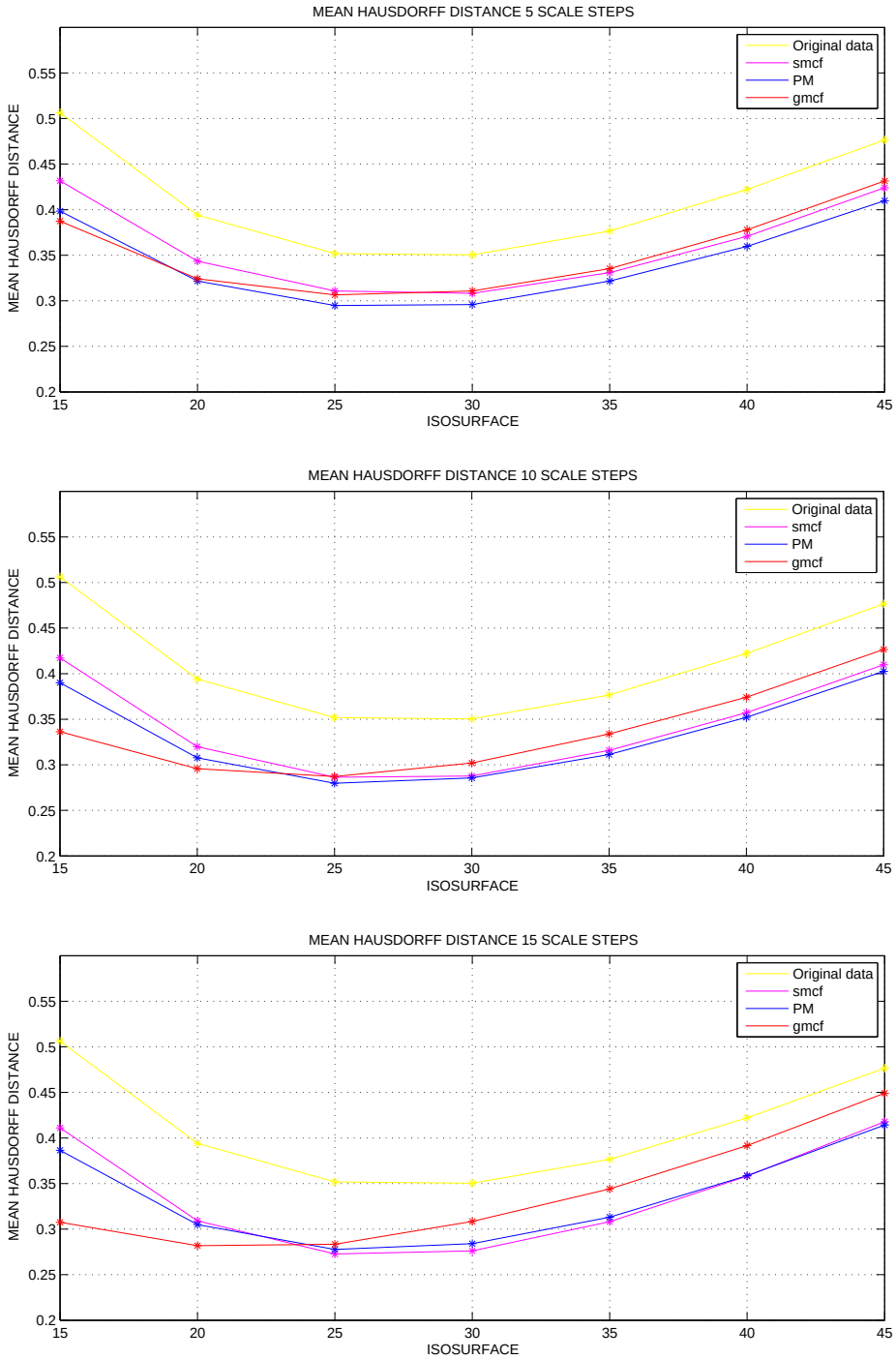

Fig. 8. Graphs of the mean Hausdorff distances for the original and filtered data using the same settings of parameters ($K = 1, \sigma = 0.0001, \tau = 0.0001$) after 5, 10 and 15 time steps (from top to bottom).

and data filtered by different methods. Two of the nuclei have a relatively regular shape, while the outline of the third, bottom-right one, is jagged. Figure 7 represents the graphs of the image intensity in a line neighborhood

of nucleus that are useful to evaluate ability of the methods to smooth the small variations in the image intensity and preserve or even enhance the edge information.

Table 2
The mean Hausdorff distances and their standard deviation for the original data. Values are in μm.

Isosurface	mean Hausdorff distance
15	0.506 ± 0.085
20	0.394 ± 0.063
25	0.352 ± 0.025
30	0.350 ± 0.035
35	0.377 ± 0.062
40	0.422 ± 0.088
45	0.476 ± 0.112

We also present in Table 4 the number of detected regions, and in Tables 2 and 3 and Figure 8 the values and graphs of the mean Hausdorff distances to the gold standard for every selected isosurface value. In Tables 2 and 3 we give also a standard deviation of the mean Hausdorff distance averaged over 11 nuclei in the gold standard. From Table 2 we can easily conclude that our choice of isosurface value 28 as the closest to the "real" boundaries of nuclei was reasonable. In the original data, the isosurfaces with values between 25 and 30 give the smallest (and approximately the same) mean Hausdorff distance to the gold standard. This fact is expressed in the almost flat graph of the mean Hausdorff distance, see Figure 8, in this interval. It is worth noting that the interval of the flatness for original data is very narrow (in contrast to the graphs using PM, SMCF and GMCF filtering results) which means that correct representation of nuclei in noisy data is very sensitive to the choice of correct isosurface level. Now, let us discuss in detail the behavior of the filtering methods. Obviously, the mean curvature flow needs a smaller time step than the other methods. In Figure 6, its contour line 28, plotted in green, is entirely inside the nuclei with regular shape already after 5 time steps, and it is completely absent in the third bottom-right one. After 15 time steps this isoline disappears in all three nuclei. Figure 7 illustrates reduction of image intensity by this model, and Tables 3 and 4 show that after 10 or 15 time steps the Hausdorff distances are really large and many isosurfaces which should represent nuclei are completely lost. This was also the reason not to include the graph for MCF in Figure 8. The results of the Perona-Malik model and the slowed mean curvature flow look very similar. Their level lines are often overlapped and both are able to remove the spurious regions very well. Their

Table 3
The mean Hausdorff distances and their standard deviation in μm for the data filtered using the same settings of parameters after 5,10 and 15 time steps ($K = 1, \sigma = 0.0001, \tau = 0.0001$).

The mean Hausdorff distances after 5 time steps

Isosurface	MCF	SMCF	PM	GMCF
15	0.357 ± 0.058	0.432 ± 0.091	0.398 ± 0.085	0.387 ±0.088
20	0.461 ± 0.120	0.344 ± 0.060	0.322 ± 0.060	0.324 ±0.053
25	0.594 ± 0.170	0.311 ± 0.028	0.295 ± 0.028	0.307 ±0.026
30	0.738 ± 0.203	0.308 ± 0.034	0.296 ± 0.030	0.310 ±0.040
35	0.887 ± 0.229	0.331 ± 0.064	0.322 ± 0.063	0.335 ±0.069
40	1.043 ± 0.253	0.371 ± 0.087	0.360 ± 0.084	0.378 ±0.092
45	1.207 ± 0.277	0.424 ± 0.106	0.410 ± 0.099	0.431 ±0.108

The mean Hausdorff distances after 10 time steps

Isosurface	MCF	SMCF	PM	GMCF
15	0.841 ± 0.258	0.417 ± 0.106	0.390 ± 0.096	0.336 ± 0.091
20	1.084 ± 0.323	0.320 ± 0.069	0.308 ± 0.068	0.296 ± 0.052
25	1.323 ± 0.374	0.286 ± 0.030	0.280 ± 0.028	0.287 ± 0.031
30	1.567 ± 0.423	0.288 ± 0.038	0.286 ± 0.031	0.302 ± 0.054
35	1.822 ± 0.478	0.316 ± 0.065	0.311 ± 0.064	0.334 ± 0.077
40	2.097 ± 0.547	0.357 ± 0.085	0.352 ± 0.084	0.374 ± 0.090
45	2.407 ± 0.618	0.410 ± 0.096	0.403 ± 0.095	0.426 ± 0.100

The mean Hausdorff distances after 15 time steps

Isosurface	MCF	SMCF	PM	GMCF
15	1.622 ± 0.558	0.411 ± 0.117	0.386 ± 0.102	0.308 ± 0.087
20	2.034 ± 0.679	0.309 ± 0.078	0.305 ± 0.073	0.282 ± 0.049
25	2.490 ± 0.848	0.273 ± 0.039	0.278 ± 0.029	0.283 ± 0.039
30	3.204 ± 1.208	0.276 ± 0.043	0.284 ± 0.034	0.308 ± 0.060
35	-	0.308 ± 0.067	0.313 ± 0.065	0.344 ± 0.078
40	-	0.358 ± 0.078	0.359 ± 0.084	0.392 ± 0.087
45	-	0.418 ± 0.090	0.414 ± 0.098	0.449 ± 0.096

Table 4
The number of regions for different isosurfaces found in the original and filtered data using the same settings of parameters ($K = 1, \sigma = 0.0001, \tau = 0.0001$).

Regions found after 5 time steps

Isosurface	original	MCF	SMCF	PM	GMCF
15	1690	14	21	12	17
20	756	11	16	11	17
25	342	11	17	13	14
30	171	11	16	13	15
35	129	11	19	16	18
40	100	11	17	16	16
45	97	11	23	18	21

Regions found after 10 time steps

Isosurface	original	MCF	SMCF	PM	GMCF
15	1690	11	11	11	11
20	756	11	11	11	11
25	342	11	11	11	11
30	171	11	11	11	12
35	129	11	11	12	11
40	100	11	11	12	11
45	97	12	14	12	13

Regions found after 15 time steps

Isosurface	original	MCF	SMCF	PM	GMCF
15	1690	11	11	11	11
20	756	11	11	11	11
25	342	12	11	11	11
30	171	13	11	11	11
35	129	7	11	11	11
40	100	5	11	11	11
45	97	5	11	11	12

graphs of mean Hausdorff distances are almost parallel to the graph of original data, meaning that both methods are able to smooth the small image intensity variations preserving at the same time a good definition of edges. Nevertheless, the Perona-Malik model shows a slightly stronger capability of smoothing and sharpening. Observing carefully Figure 6, we can see that for the convex parts of image contours, the blue line (PM result) is inside the magenta one (SMCF result), while for the concave parts, the behavior is opposite. The slight edge sharpening can be deduced observing the graphs and the values of the mean Hausdorff distances. After 5 time steps, the shapes of the graphs looks very similar, although the SMCF graph is completely above the PM result. Increasing the time, the graph of the SMCF approaches that of PM, but their behavior is different. After 15 time steps the PM graph is less convex and slightly more flat for lower isosurfaces, meaning that the Perona-Malik method tends to accumulate more the image gray levels in that range of image intensity. This kind of behavior is dominant in the geodesic mean curvature flow model, that completely flattens the region of a low intensity, thus enhancing the edge positions around nuclei. In Figure 7, the red line representing GMCF is totally flat outside the nucleus, and among all the methods, it has the lowest values near the nucleus boundaries. The level lines reproduce very tightly the shape of nuclei, see Figure 6, but they are always the most internal. The graph of the mean Hausdorff distance is completely different from the others. It is almost flat up to the isosurface value 25, then it is parallel to the graph of the original data. We can deduce that this method changes the original distribution of the image gray levels producing an image sharpening, although slightly shrinking the objects. To conclude this subsection, we also observe that the GMCF, similarly to PM and SMCF models, is capable of removing the spurious regions very well, cf. Table 4.

4.3 Comparison of the filtering methods with the optimally chosen parameters

By extensively testing computational methods for the studied PDE models, we decided to choose as the optimal parameters the ones giving the lowest and the flattest graph of the mean Hausdorff distance. We paid attention not only to the minimal distance between the best isosurface and the gold standard but also to the whole range of distances around the best value. In all the methods we use $h = 0.01$ and the optimally chosen parameters are listed in Table 5.

For the GMCF filter we used as optimal parameters those chosen in the previous subsection taking number N of time steps equal to 15. Indeed, we observed that reducing σ gives a similar graph of MHD, but with bigger distances, while increasing it produces loss of information. A smaller value of K further flat-

Table 5
The optimal parameters for different models. In the last row we present the computational times for such settings of parameters.

	MCF	SMCF	PM	GMCF
τ	0.00001	0.0001	0.0001	0.0001
σ	-	0.00005	0.00005	0.0001
K	-	0.5	0.5	1
N	5	10	10	15
CPU time	95.97 s	263.22 s	119.44 s	386.54 s

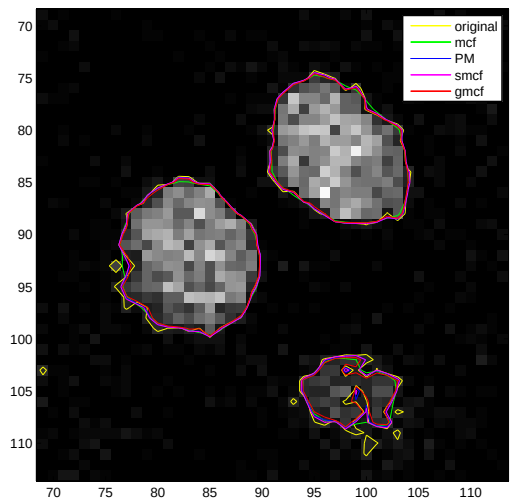

Fig. 9. A 2D cut of original data with cut of the isosurface 28 of original and filtered data using the optimal values of parameters (cf. Table 5).

tens the graph for low isosurface levels but increases the slope of the others, a bigger value of K makes the graph more convex. Since the smoothing effect of MCF method is very fast, we use ten times smaller discrete time step τ and we choose $N = 5$. The SMCF and PM methods show a very good behavior after 10 time steps, and we found useful to slightly modify the values of K and σ. The new values and graphs of the mean Hausdorff distances are presented in Table 6 and in Figure 10. We also evaluated the methods by visual inspection, cf. Figures 9, 11 and 12 .

First of all, the mean curvature flow is the method that gives the minimum value of the mean Hausdorff distance for the isosurface value 25, cf. Table 6. It has the highest smoothing capability in a small range of gray levels around this value, as also observed form the smooth shape of nuclei in Figures 11 and 12. However, from the strongly convex graph in Figure 10, it is easy to see

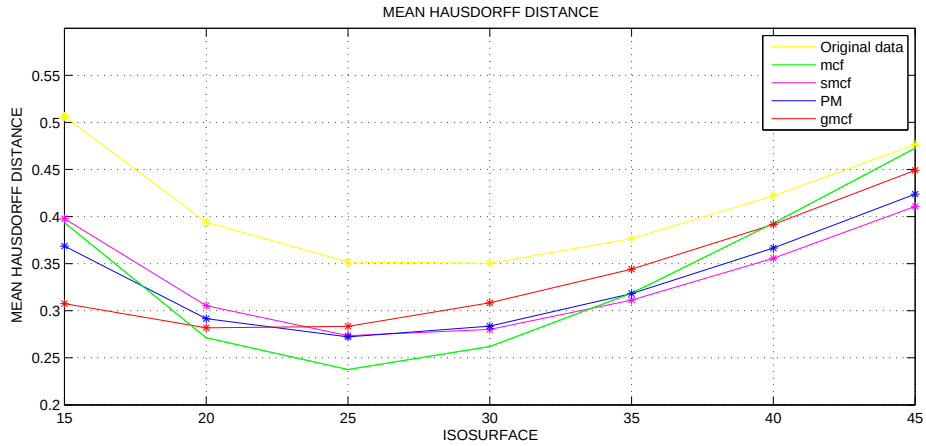

Fig. 10. Graphs of the mean Hausdorff distances for the original data and data filtered using the optimal values of parameters (cf. Table 5).

Table 6
The mean Hausdorff distances and their standard deviation in μm for the filtered data using the optimal values of parameters (cf. Table 5).

	Mean Hausdorff Distance			
Isosurface	MCF	SMCF	PM	GMCF
15	0.394 ± 0.100	0.411 ± 0.107	0.369 ± 0.089	0.308 ± 0.087
20	0.271 ± 0.072	0.302 ± 0.072	0.292 ± 0.054	0.282 ± 0.049
25	0.238 ± 0.026	0.265 ± 0.033	0.272 ± 0.020	0.283 ± 0.039
30	0.262 ± 0.048	0.274 ± 0.039	0.284 ± 0.042	0.308 ± 0.060
35	0.319 ± 0.086	0.313 ± 0.068	0.318 ± 0.070	0.344 ± 0.078
40	0.393 ± 0.106	0.364 ± 0.083	0.367 ± 0.086	0.392 ± 0.087
45	0.473 ± 0.117	0.429 ± 0.095	0.424 ± 0.095	0.449 ± 0.096

that this method completely changes the distribution of the image gray levels thus modifying the shape of the objects. Without using an edge information, the method moves the level sets of the image with a speed given by their curvature, smoothing fast the regions near the nuclei boundaries that should be preserved and smoothing slowly the regions with low intensity gradient that should be removed from the image. Consequently, Table 7 shows that this method preserves spurious regions characterized by a low level of brightness.

Similarly to the previous subsection, analyzing the graphs of the mean Hausdorff distances, we conclude that the Perona-Malik method produces a little sharpening in a similar way as the geodesic curvature method, while the slowed

Table 7
The number of regions found in the original and filtered data using the optimal choice of parameters (cf. Table 5).

Regions found using the optimal values of parameters					
Isosurface	original	MCF	SMCF	PM	GMCF
15	1690	19	11	11	11
20	756	12	11	11	11
25	342	11	11	11	11
30	171	11	11	11	11
35	129	11	11	11	11
40	100	11	11	11	11
45	97	11	11	11	12

mean curvature flow performs a pure edge preserving smoothing. Such behavior can be observed also by visual inspection. Figure 12 shows, on the left, a detail of the nuclei very close in the original data. While the sharpening is completely absent in the results obtained using the slowed mean curvature flow, it increases from the Perona-Malik to the geodesic curvature method, which is able to correctly divide the nuclei. In next section we analyze thoroughly and quantitatively evaluate this particular aspect.

4.4 Comparison of filtering models using their ability of splitting adjacent nuclei

In the previous sections we showed that the geodesic mean curvature flow is the method that best enhances the nuclei edges. The image gray levels outside the nuclei boundaries are smoothed while those around the boundaries accumulate to form a step between the outward and the inward part of every nucleus. Such a behavior allows to distinguish between two (or more) regions that are connected due to acquisition errors intrinsically linked to LSM. In order to quantify this *ability of splitting* the connected nuclei, we first filtered with the parameters shown in Table 5 a selected volume in the time lapse series. Then we considered the isosurface 28 (see section 4.2) of original and filtered data for nuclei representation. A manual counting of connected components in original data revealed that 45 nuclei are connected with another nucleus, giving rise to 22 connected regions (that is, 42 nuclei are joint two by two to form 21 regions and three nuclei are joint to form one region). Every double or triple region has been checked after the filtering. While the geodesic curvature flow is able to divide half of the connected regions, the Perona-Malik method performs only

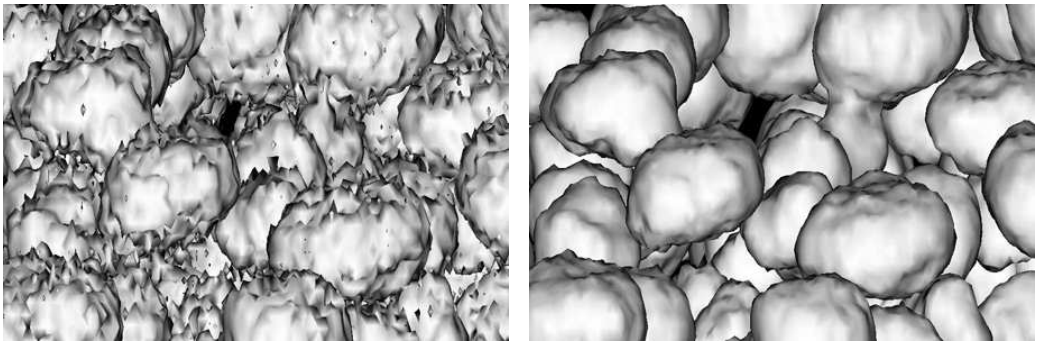

(a) Original data (b) Mean curvature flow

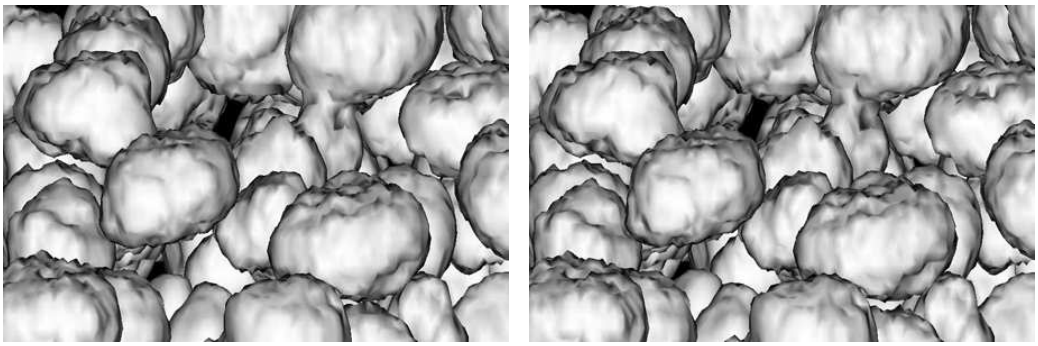

(c) Slowed mean curvature flow (d) Perona-Malik

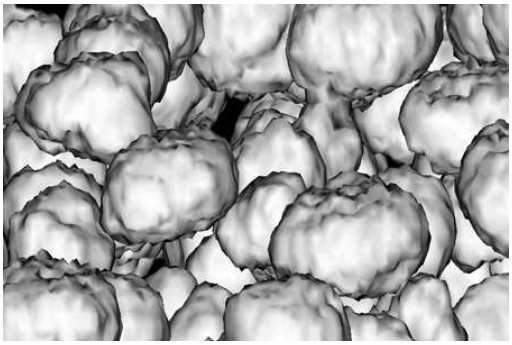

(e) Geodesic mean curvature flow

Fig. 11. Isosurface representation of original (a) and filtered data (by isosurface value 28) using optimal parameters (b-e). Parameters are given in Table 5.

four divisions, the mean curvature flow two and the slowed mean curvature flow only one. An example is shown in Figure 12 and results are summarized in Table 8.

4.5 Comparison with the tensor nonlinear diffusion and Beltrami flow

In the previous sections we analyzed carefully the behavior of specific nonlinear diffusion models applied to our data. The GMCF filter showed the best properties. In this section we compare such method with other well known

Table 8
The number of connected regions found in original and filtered data using the optimal choice of parameters , as given in Table 5.

Connected regions number				
Original	MCF	SMCF	PM	GMCF
22	20	21	18	11

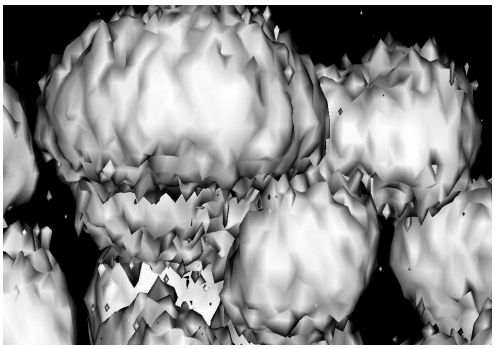

(a) Original data

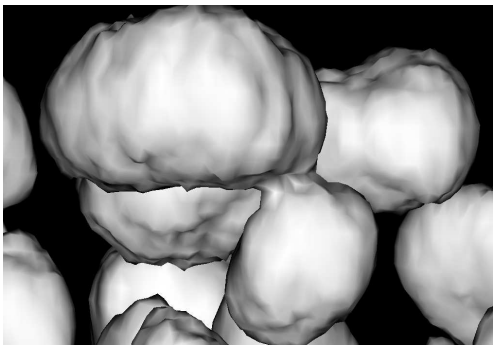

(b) Mean curvature flow

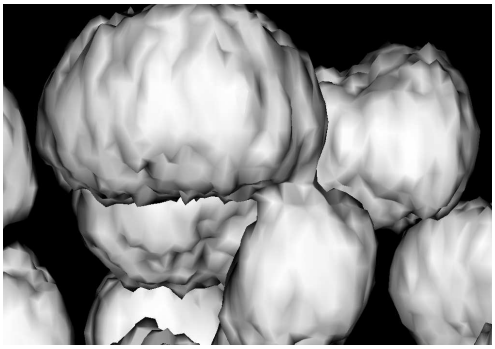

(c) Slowed mean curvature flow

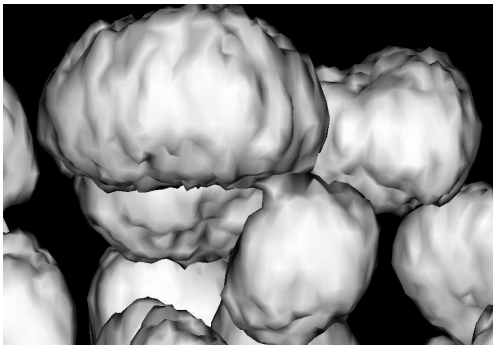

(d) Perona-Malik

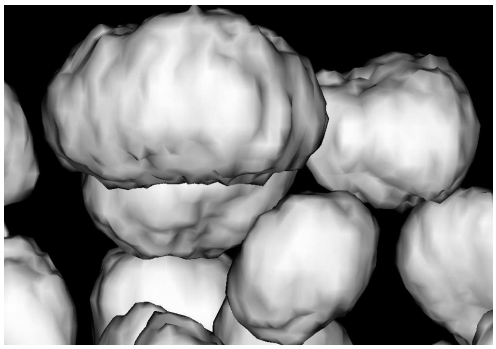

(e) Geodesic mean curvature flow

Fig. 12. Isosurface representation of original (a) and filtered data (by isosurface value 28) using optimal parameters,as shown in Table 5 (b-e). The Geodesic mean curvature flow is able to distinguish between two very close nuclei.

nonlinear diffusion filtering methods, the tensor nonlinear diffusion (TND) and the Beltrami flow method. In both cases we evaluate the results using the criteria previously introduced, based on visual inspection and quantitative analysis. In particular the parameters have been still chosen according to the best combination between the graph of MHD and the number of regions detected. The results are compared with those obtained with GMCF.

The tensor nonlinear diffusion (TND), introduced in Weickert (1999), is given by the equation

$$u_t - \nabla \cdot (D \nabla u) = 0 \tag{40}$$

where D is a diffusion tensor (matrix). This model is used when a strong smoothing is desirable in a preferred direction, e.g. along 2D edge surfaces in 3D images and a low smoothing is expected in the perpendicular direction. If the diffusion tensor D is properly designed, the model has the property to improve the spatial coherence of structures, cf. Weickert (1999); Drblíková & Mikula (2007a,b). For the tests we use 3D finite volume method for TND, based on the similar discretization principles as described in this paper, which was introduced in Drblíková & Mikula (2007b). We discuss below how TND behaves for the nuclei images in 3D embryogenesis data sets. By an extensive testing we found the optimal TND parameters with respect to the Hausdorff distance. They are given by 3 filtering steps with a time step 10^{-5} and other parameters as follows: $\sigma = 10^{-5}, \rho = 5 \cdot 10^{-3}, \alpha = 10^{-3}$, where additionally to our models, ρ represents a spatial Gaussian smoothing of coherence directions and α gives the a diffusion in a perpendicular direction, cf. Drblíková & Mikula (2007b).

Examining the graph of the MHD in Figure 13 we first observe that the distances are strongly reduced in the range between isosurfaces 25 and 45, while for smaller isosurface values the distances are bigger that those of original data. The graph shape is generally strongly convex and shows some flatness only between isosurfaces 30 and 35. The behavior is then excellent in the regions inside nuclei, after isosurface 30, but is poor outside them. The method performs a very good smoothing but does not perform any sharpening. Furthermore it tends to enlarge the nuclei. When a surface is jagged (e.g. thinking in 1D, given by a sequence of peaks and valleys, as shown in Figure 14), it tends to fill the valleys more than to smooth and lower the peaks. As a consequence it does not offer any ability of splitting adjacent nuclei. None of the 22 connected regions in the original data was split after the filtering and the number of connected regions even increased to 29. The smoothed shape of nuclei surface after the filtering and the small increasing of volume can be observed in Figure 15.

The Beltrami flow method (Sochen et al., 1995; Kimmel et al., 1996) considers the images as embedding maps flowing towards minimal surfaces. The motion equation can be explicitly given, in the three dimensional case, by the following

expression

$$u_t = H/\sqrt{h} \tag{41}$$

where H is the mean curvature of the graph of subsequently smoothed image intensity u and $h = 1 + u_x^2 + u_y^2 + u_z^2$. The method performs a selective mean curvature filtering for the image graph, which is smoothed only in the direction given by the last component of the embedding space, the image intensity. The Beltrami flow has a wide and rigorous mathematical treatment showing that it is a solution of a minimization problem with a particular choice of image metric. For further details we refer the reader e.g to Sochen et al. (1995, 2003). Since the equation (41) can be written in the form $u_t = \frac{1}{h}\sqrt{h}H$, we can see that its structure is similar to (10) with the edge indicator function $g = 1/h$. Then one can easily derive semi-implicit finite volume scheme, cf. (19) and (34), which is used for our tests. The best results with respect to Hausdorff distance we found for the Beltrami flow using 15 scale steps with a time step 0.0001 and they are summarized in Figures 13,14,15 and Tables 9,10.

The shape of the MHD reveals that the method is edge-preserving and even performs a small sharpening. The curve of the graph in the range between isosurfaces 15-30 is almost parallel to the curve related to the original data. The range 20-30 is almost flat and the MHD between filtered and original data for isosurface 15 is bigger than for isosurface 20. Inside the nuclei the Beltrami flow performs a pure edge-preserving smoothing. Such behavior is confirmed by our splitting analysis, as on the 22 connected regions in the original data only one is split after the filtering, in a similar way as PM and SMCF methods. Despite this, the method does not seem to be able to distinguish between the biggest regions representing the nuclei and the smallest corresponding to the noise, as shown in Table 10. Moreover, observing Figure 14, it can be seen how the method well reproduces the shape of internal regions but cannot easily distinguish between regions of low and mean intensity. As a further consequence the isosurface shape shown in Figure 15 appears more irregular than in the case of other filtering methods. We tested that increasing the number of scale steps in order to detect the correct number of regions produces a very convex MHD graph and the method loses its ability to preserve-enhance the edges. In particular, the MHD for low isosurfaces is bigger than for the original data. To conclude this section, we observed that considering a modified edge indicator $g = 1/h$ in which the modulus of squared image gradient $|\nabla u|^2$ is convolved with a Gaussian kernel with small variance ($\sigma = 0.00005$), the basic properties of the Beltrami flow are preserved but the ability to detect the correct number of regions is improved. Related results are summarized in Figures 16, 17, 18 and Tables 11, 12.

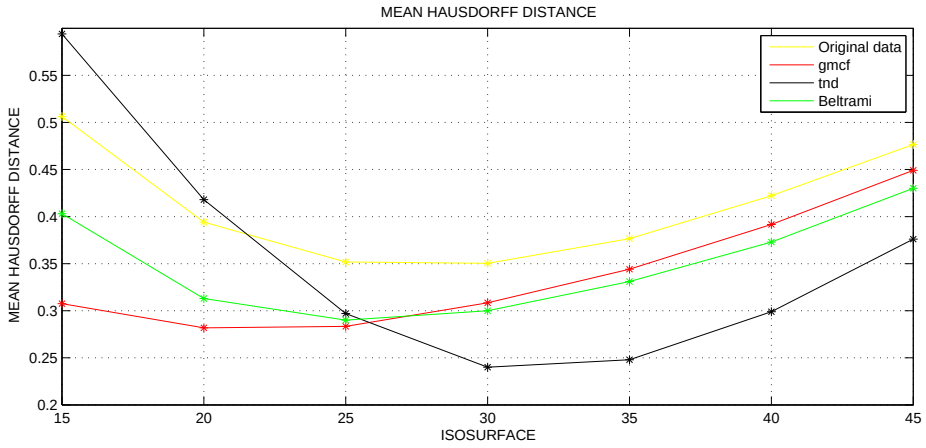

Fig. 13. Graph of the MHD comparing original, geodesic mean curvature flow, tensor diffusion and Beltrami flow filtered data.

Table 9
Comparison between geodesic mean curvature flow, tensor diffusion and Beltrami flow. Error expressed as the mean Hausdorff distance with its standard deviation. Distances in μm for original and filtered data.

Mean Hausdorff Distance

Isosurface	Original	GMCF	TND	BELTRAMI
15	0.506 ± 0.085	0.308 ± 0.087	0.594 ± 0.077	0.403 ± 0.086
20	0.394 ± 0.063	0.282 ± 0.049	0.418 ± 0.079	0.313 ± 0.050
25	0.352 ± 0.025	0.283 ± 0.039	0.297 ± 0.067	0.290 ± 0.023
30	0.350 ± 0.035	0.308 ± 0.060	0.240 ± 0.031	0.300 ± 0.037
35	0.377 ± 0.062	0.344 ± 0.078	0.248 ± 0.036	0.331 ± 0.065
40	0.422 ± 0.088	0.392 ± 0.087	0.299 ± 0.074	0.373 ± 0.088
45	0.476 ± 0.112	0.449 ± 0.096	0.376 ± 0.096	0.430 ± 0.101

5 Conclusions

We applied the methods of nonlinear diffusion filtering to 3D LSM images of cell nuclei during zebrafish embryogenesis, characterized by a low resolution in z-direction (deepness) giving rise to partially overlapped regions. Our goal was to identify the best filtering method and improve its numerical scheme in order to facilitate further image processing procedures, as nuclei identification, segmentation and tracking. To that aim we first improved known finite volume schemes for solving the regularized Perona-Malik equation, and classical, slowed and geodesic mean curvature flow equations, by speeding up the computations and improving accuracy. Then we studied the behavior of all the

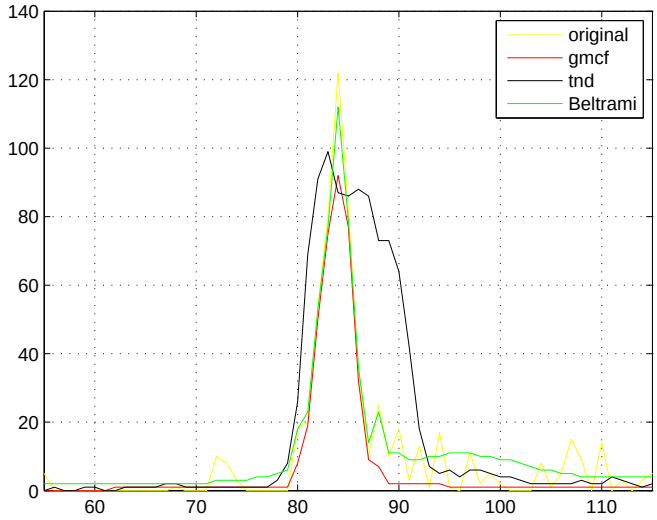

Fig. 14. Plot of original and filtered (gmcf, tnd and Beltrami) image intensities in a neighborhood of one of the nuclei from Figure 6.

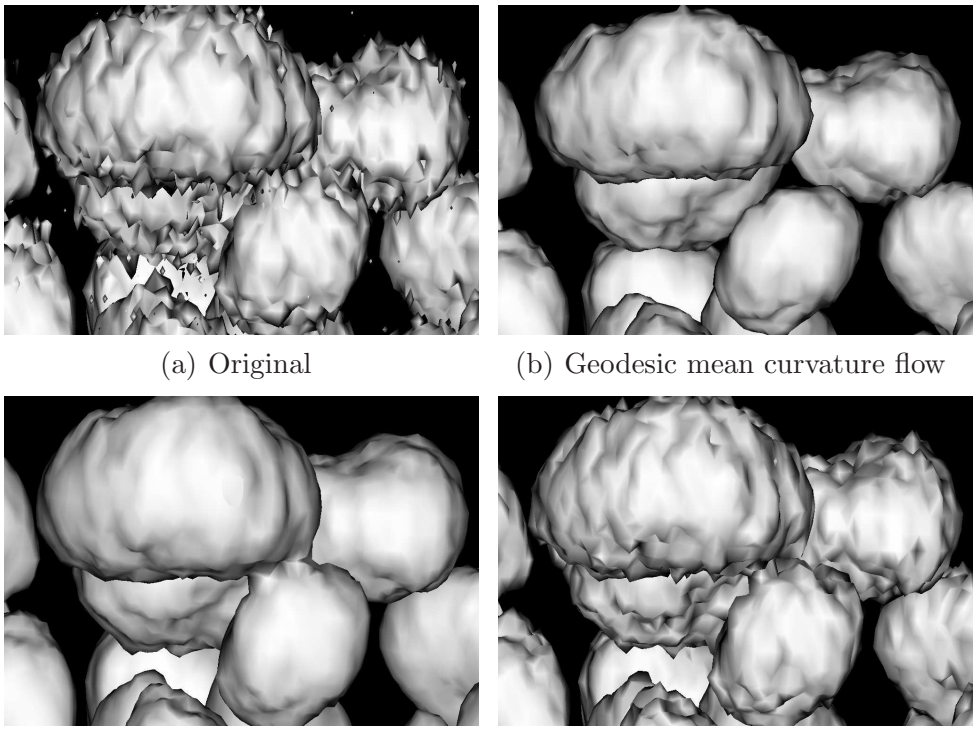

(a) Original (b) Geodesic mean curvature flow

(c) Tensor diffusion (d) Beltrami flow

Fig. 15. Isosurface of original (a) and filtered data (by isosurface value 28) comparing the geodesic mean curvature flow, the tensor diffusion and the Beltrami flow methods (b-d). The point of view is the same as in Figure 12.

Table 10
The number of regions found in the original and filtered data comparing geodesic mean curvature flow, tensor diffusion and Beltrami flow.

	Regions found			
Isosurface	Original	GMCF	TND	BELTRAMI
15	1690	11	11	15
20	756	11	11	14
25	342	11	11	16
30	171	11	11	20
35	129	11	11	24
40	100	11	11	28
45	97	12	11	35

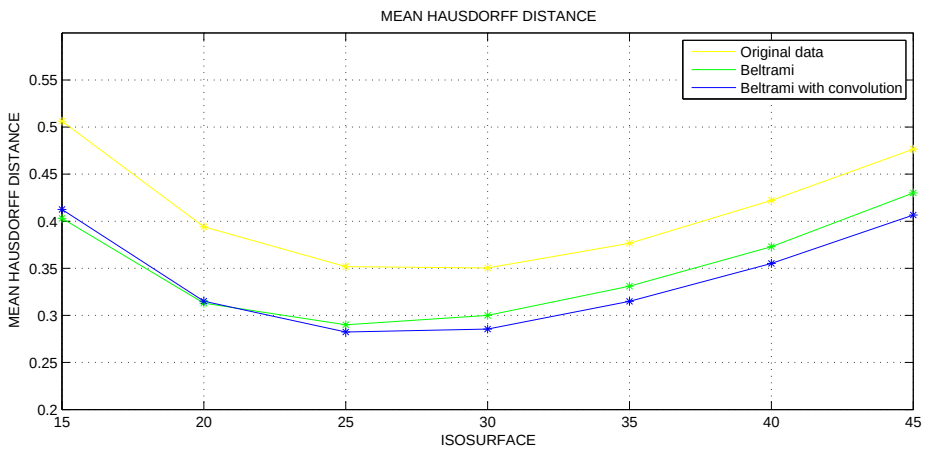

Fig. 16. Graph of the MHD comparing results obtained by Beltrami filtering with and without a Gaussian convolution.

methods and evaluated their performances both visually and quantitatively. The quantitative analysis has been carried out first by calculating the mean Hausdorff distance of isosurfaces to a gold standard and by quantifying the number of regions detected applying every method, then by counting the number of originally connected regions that can be split with the filtering step. Such *ability of splitting* is essential to assure, in this particular typology of data, a correct nuclei detection in subsequent image processing operations.

We showed that our numerical schemes, based on common discretization principles (finite volume method in space and semi implicit method in time) are fast, accurate and unconditionally stable. The unconditional stability provides the robustness of methods and is especially important for solving the mean curvature flow like problems. We proved that the nonlinear diffusion filtering is efficient and robust in increasing the range of isosurfaces suitable for

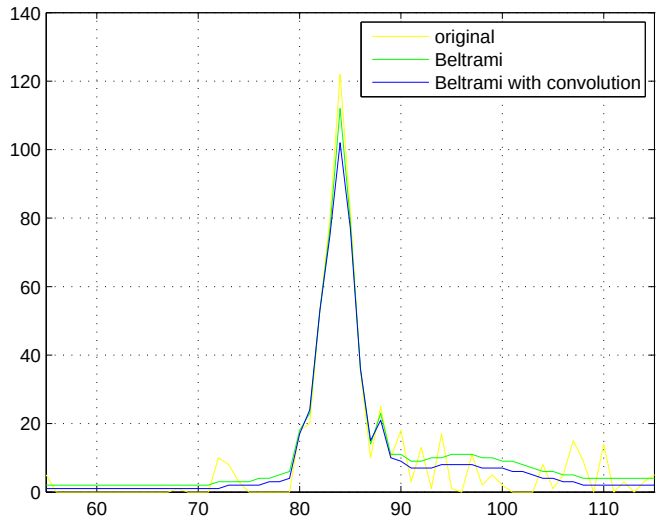

Fig. 17. Graphs of filtered image intensities in a neighborhood of one of the nuclei from Figure 6 to compare the Beltrami flow with and without a Gaussian convolution.

Table 11
Comparison of the Beltrami flow with and without a Gaussian convolution. Error expressed as the mean Hausdorff distance with its standard deviation. Distances in μm for original and filtered data.

	Mean Hausdorff Distance		
Isosurface	Original	BELTRAMI	conv.BELTRAMI
15	0.506 ± 0.085	0.403 ± 0.086	0.413 ± 0.106
20	0.394 ± 0.063	0.313 ± 0.050	0.315 ± 0.067
25	0.352 ± 0.025	0.290 ± 0.023	0.282 ± 0.029
30	0.350 ± 0.035	0.300 ± 0.037	0.285 ± 0.037
35	0.377 ± 0.062	0.331 ± 0.065	0.315 ± 0.065
40	0.422 ± 0.088	0.373 ± 0.088	0.355 ± 0.085
45	0.476 ± 0.112	0.430 ± 0.101	0.407 ± 0.098

localizing the nuclei. Thanks to the introduction of the use of the mean Hausdorff distance to evaluate the behavior of filtering methods around the object boundaries, we quantified the smoothing and sharpening capabilities of every model. We showed that all the analyzed methods are able to reduce the noise, smooth small variations in image intensity of the original data and remove the spurious regions. For the Perona-Malik, slowed and geodesic mean curvature flow models, the filtering reduces the mean Hausdorff distance significantly

Table 12
The number of regions found in the original and filtered data comparing Beltrami flow with and without a Gaussian convolution.

	Regions found		
Isosurface	Original	BELTRAMI	conv.BELTRAMI
15	1690	15	11
20	756	14	11
25	342	16	11
30	171	20	11
35	129	24	11
40	100	28	11
45	97	35	12

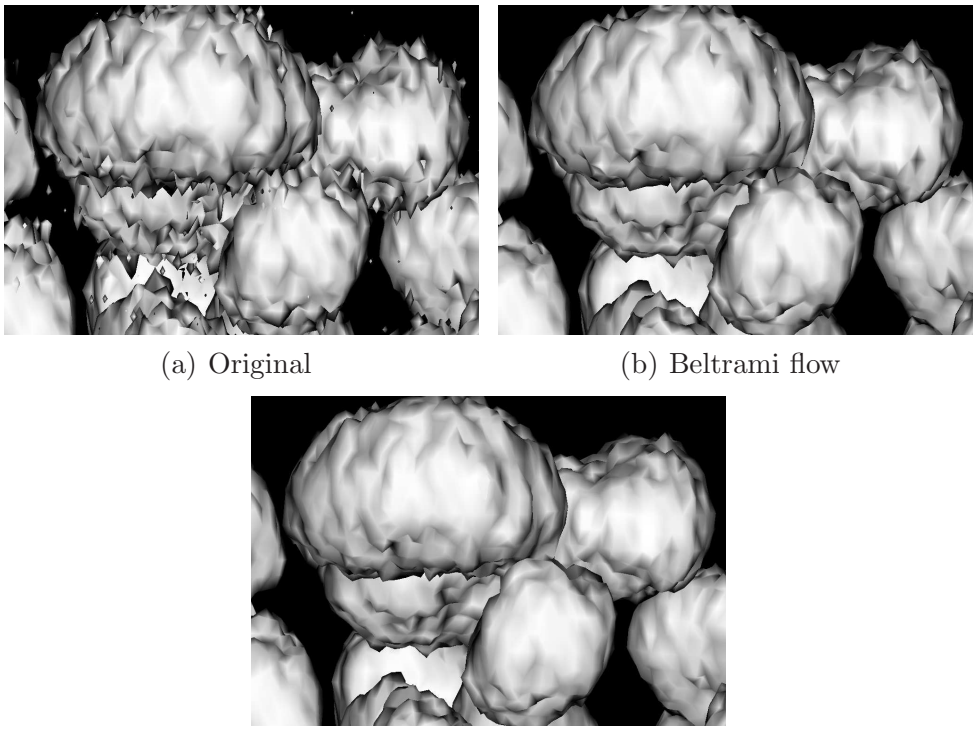

(a) Original (b) Beltrami flow

(c) Beltrami with convolution

Fig. 18. Isosurface of original (a) and filtered data (by isosurface value 28) comparing Beltrami flow with and without a Gaussian convolution. The point of view is the same as in Figures 12 and 15.

for a large range of isosurfaces, and it always extracts the correct number of connected components of isosurface corresponding to the number of nuclei in a tested subvolume of data. The geodesic mean curvature flow model shows also the capability of sharpening, flattening the graph of the mean Hausdorff distance on the boundaries of imaged nuclei. Such behavior produces an other

very welcome effect, that is the ability of splitting the artificially connected subregions, almost absent in the other evaluated models. These results identify the geodesic mean curvature flow as the best suited for this particular application. Our choice is also supported by a qualitative and quantitative comparison with two other well known nonlinear diffusion filtering methods, the nonlinear tensor diffusion and the Beltrami flow. Both of them do not show characteristics useful to treat the LSM nuclei data.

6 ACKNOWLEDGMENTS

This work was supported by the European projects Embryomics (NEST 012916), BioEmergences (NEST 028892), Computer Vision Foundations and Applications (Alfa II-0366-FA), and grants VEGA 1/0269/09, APVV-0351-07, APVV-RPEU-0004-06, APVV-LPP-020-07. We thank all the members of the projects for our very fruitful interdisciplinary interaction.

References

Alvarez, A., Guichard F., Lions P. L., & Morel, J.M., Axioms and Fundamental Equations of Image Processing, Archive for Rat. Mech. Anal., 1993, 123, 200-257.

Alvarez, A., Lions, P. L., & Morel, J.M., Image selective smoothing and edge detection by nonlinear diffusion II, SIAM J. Numer. Anal., 1992, 29, 845-866.

Bruhn, A., Jakob, T., Fisher, M., Kohlberger, T., Weickert, J., Brüning, U., & Schnörr, C., High performance cluster computing with 3D nonlinear diffusion filters, Real-Time Imaging, 2004, 10, 41-51.

Cao F., Application of the Gestalt principles to detection of good continuations and corners in image level lines, Computing and Visualization in Science, 2004, 7, 3-13.

Catté, F., Lions, P.L., Morel, J.M., & Coll, T., Image selective smoothing and edge detection by nonlinear diffusion, SIAM J. Numer. Anal., 1992, 29, 182-193.

Chen, Y., Vemuri, B.C., & Wang, L., Image denoising and segmentation via nonlinear diffusion, Computers and Mathematics with Applications, 2000, 39, 131-149.

Caselles, V., Kimmel, R., & Sapiro, G., Geodesic active contours, International Journal of Computer Vision, 1992, 22, 61-79.

Caselles, V., Kimmel, R., Sapiro, G., & Sbert, C., Minimal surfaces: a geometric three dimensional segmentation approach, Numer. Math., 1997, 77, 423-451.

Crandall, M.G., Ishii, H., & Lions, P.L., User's guide to viscosity solutions of second order partial differential equations, Bull. Amer. Math. Soc. (NS), 1992, 27, 1-67.

Corsaro, S., Mikula, K., Sarti, A., & Sgallari, F., Semi-implicit co-volume method in 3D image segmentation, SIAM Journal on Scientific Computing, 2006, 28, 6, 2248-2265.

Coudiere, Y., Vila, J. P., & Villedieu, P., Convergence rate of a finite volume scheme for a two-dimensional convection-diffusion problem, M2AN Math. Model. Numer. Anal., 1999, 33, 493-516.

Deckelnick, K., & Dziuk, G., Error estimates for a semi implicit fully discrete finite element scheme for the mean curvature flow of graphs, Interfaces and Free Boundaries, 1999, 2, 4, 341-359.

Drbliková, O., Komorniková, M., Mikula, K., Peyriéras, N., & Remešiková M., Estimate of the cell growth rate using image processing and time series analysis, Journal of Electrical Engineering, 2007, 7/s, 58, 86-92.

Drblíková, O., & Mikula, K., Convergence Analysis of Finite Volume Scheme for Nonlinear Tensor Anisotropic Diffusion in Image Processing, SIAM Journal on Numerical Analysis, 2007, 46, 1, 37-60.

Drblíková, O., & Mikula, K., Semi-implicit diamond-cell finite volume scheme for 3D nonlinear tensor diffusion in coherence enhancing image filtering, in Finite Volumes for Complex Applications V: Problems and Perspectives (Eds. R.Eymard, J.M.Herard), ISTE and WILEY, London, 2008, 343-350.

Dufour, A. et al., Segmentation and tracking fluorescent cells in dynamic 3D microscopy with coupled active surfaces, IEEE Trans. Image Processing, 2005, 14, 1396-1410

Evans, L.C., & Spruck J., Motion of level sets by mean curvature I, J. Differential Geometry, 1991, 33, 635-681.

Eymard, R., Gallouet, T., & Herbin R., The finite volume method, Handbook for Numerical Analysis, 2000, 7 (Ph. Ciarlet, J. L. Lions, eds.), Elsevier.

Fischer, B., & Modersitzki J., Fast diffusion registration, AMS Contemporary Mathematics, Inverse Problems, Image Analysis and Medical Imaging, 2002, 313, 117-129.

Frolkovič, P., Mikula, K., Peyriéras N., & Sarti A., A counting number of cells and cell segmentation using advection-diffusion equations, Kybernetika, 2007, 43 (6), 789-796.

Handlovičová, A., and Z. Krivá, Error estimates or finite volume scheme for Perona-Malik equation, Acta Math. Univ. Comenianae, 2005, 74 (1) 79-94.

Handlovičová, A., & Mikula, K., Stability and consistency of the semi-implicit co-volume scheme for regularized mean curvature flow equation in level set formulation, Applications of Mathematics, 2008, 53 (2) 105-129.

Handlovičová, A., Mikula, K., & Sgallari, F., Variational numerical methods for solving nonlinear diffusion equations arising in image processing, J. Visual Communication and Image Representation, 2002, 13. 217-237.

Handlovičová, A., Mikula, K., & Sgallari, F., Semi-implicit complementary volume scheme for solving level set like equations in image processing and

curve evolution, Numer. Math., 2003, 93, 675-695.

Huttenlocher, D.P., Klanderman, G.A., & Rucklidge, W.J., Comparing Images using the Hausdorff Distance, IEEE Transactions on Pattern Analysis and Machine Intelligence, 1993, 15 (9) 850-863.

Kačur, J., & Mikula, K., Solution of nonlinear diffusion appearing in image smoothing and edge detection, Applied Numerical Mathematics, 1995, 17, 47-59.

Khairy, K., Reynaud, E.& Stelzer, E., Detection of deformable objects in 3D images using Markov chain, Monte Carlo and spherical harmonics, Conference Proceedings MICCAI, New York 2008.

Kichenassamy, S., Kumar, A., Olver, P., Tannenbaum, A., & Yezzi, A., Conformal curvature flows: from phase transitions to active vision Arch. Rational Mech. Anal., 1996, 134, 275-301.

Kichenassamy, S., The Perona-Malik paradox, SIAM J. Appl. Math., 1997, 57 (5) 1328-1342.

Kimmel, C.B, Ballard, W.W., Kimmel, S.R., Ullmann, B., & Schilling Th.F., Stages of embryonic development of the zebrafish Dev. Dyn., 1995, 203, 253-310.

Kimmel, R., Sochen, N., & Malladi, R., From High Energy Physics to Low Level Vision, Lectures Notes in Computer Science: First Int. Conf. Scale-Space Theory in Computer Vision, Springer-Verlag, 1997, 1252, 236-247.

Krivá, Z. & Mikula, K., Adaptive finite volume schemes in processing of 3D data sets, J. Electrical Engineering, 2001, 12/s, 52, 53-58.

Krivá, Z., & Mikula, K., An adaptive finite volume scheme for solving nonlinear diffusion equations in image processing, J. Visual Communication and Image Representation, 2002, 13, 22-35.

LeVeque, R.J., Finite Volume Methods for Hyperbolic Problems, Cambridge Texts in Applied Mathematics, Cambridge University Press, 2002.

Lin, G. et al., Hierarchical model-based merging of multiple fragments for improved three-dimensional segmentation of nuclei, Cytometry, 2005, 63A, 20-33.

Megason, S., & Fraser, S., Digitizing life at the level of the cell: highperformance laser -scanning microscopy and image analysis for in toto imaging of development, Mech. Dev., 2003, 120, 1407-1420.

Melani, C., Lombardot, B., Campana, M., Rizzi, B., Zanella, C., Bourgine, P., Mikula, K., Peyriéras, N., & Sarti, A., Cells tracking in a live zebrafish embryo, Proceedings of the 29th IEEE EMBS Annual International Conference, 2007, 23-26 Aug., Lyon, France.

Mikula, K., & Ramarosy, N., Semi-implicit finite volume scheme for solving nonlinear diffusion equations in image processing, Numer. Math., 2001, 89 (3) 561-590.

Mikula, K., & Remešikova, M., Finite volume schemes for the generalized subjective surface equation in image segmentation, Kybernetika, 2009, 45 (4) 646-656.

Mikula, K., Sarti, A., & Sgallari, F., Co-volume level set method in subjective

surface based medical image segmentation, in: Handbook of Medical Image Analysis: Segmentation and Registration Models (J. Suri et al., Eds.), Springer, New York, 2005, 583-626.

Mikula, K., & Sarti, A., Parallel co-volume subjective surface method for 3D medical image segmentation, Parametric and Geometric Deformable Models: An application in Biomaterials and Medical Imagery, Volume-II, Springer Publishers, (Eds. Jasjit S. Suri and Aly Farag), ISBN 0-387-31204-8, 2007, 123-160.

Nitzberg, M., & Shiota, T., Nonlinear image filtering with edge and corner enhancement, IEEE Trans. Pattern Analysis and Machine Intelligence, 1992, 14 (8), 826-833.

Oberman, A.M., A convergent monotone difference scheme for motion of level sets by mean curvature, Numer. Math., 2004, 99 (2), 365-379.

Osher, S., & Fedkiw, R., Level set methods and dynamic implicit surfaces, Springer-Verlag, 2003.

Perona, P., & Malik, J., Scale space and edge detection using anisotropic diffusion, Proc. IEEE Computer Society Workshop on Computer Vision, 1987.

Rizzi, B., Campana, M., Zanella, C., Melani, C., Cunderlik, R., Kriva, Z., Bourgine, P., Mikula, K., Peyriras, N., & Sarti, A., 3-D Zebrafish Embryo Image Filtering by Nonlinear Partial Differential Equations, Proceedings of the 29th Annual International Conference of the IEEE EMBS Cit Internationale, Lyon, France August 23-26, 2007.

Sapiro, G., Geometric Partial Differential Equations and Image Analysis, Cambridge University Press, 2001.

Sarti, A., Mikula, K., & Sgallari, F., Nonlinear multiscale analysis of three-dimensional echocardiographic sequences, IEEE Trans. on Medical Imaging, 1999, 18, 453-466.

Sarti, A., Mikula, K., Sgallari, F., & Lamberti C., Evolutionary partial differential equations for biomedical image processing, Journal of Biomedical Informatics, 2002, 35, 77-91.

Sarti, A., Ortiz de Solorzano, C., Lockett, S., & Malladi, R., A unified geometric model. for 3D confocal image analysis in cytology, IEEE Trans.On Biomedical Engineering, 2000, 47, 1600-1609.

Sethian, J.A., Level Set Methods and Fast Marching Methods: Evolving Interfaces in Computational Geometry, Fluid Mechanics, Computer Vision, and Material Science, Cambridge University Press, New York, 1999.

Sochen, N., Deriche, R., & Perez, L, The Beltrami Flow over Manifolds, Inria Research Report, July 2003.

Sochen, N., Kimmel, R., & Malladi, R., From high energy physics to low level vision, Report, LBNL, UC Berkeley, LBNL 39243, August, Presented in ONR workshop, UCLA, Sept.5, 1996.

Weickert, J., Romeny, B.M.t.H., &Viergever, M.A. Efficient and reliable schemes for nonlinear diffusion filtering, IEEE Trans. Image Processing, 1998, 7, 398-410.

Weickert, J., Coherence-enhancing diffusion filtering, Int. J. Comput. Vision, 1999, 31, 111-127.

Zanella, C., Rizzi, B., Melani, C., Campana, M., Bourgine, P., Mikula, K., Peyriéras, N., & Sarti, A., Segmentation of Cells from 3D Confocal Images of Live Zebrafish Embryo, Proceedings of the 29th IEEE EMBS Annual International Conference, 23-26 Aug., 2007, Lyon, France.

Zanella, C., , Campana, M., Rizzi, B., Melani, C., Sanguinetti, G., Bourgine, P., Mikula, K., Peyriéras, N., & Sarti, A., Cells Segmentation from 3D Confocal Images of Early Zebrafish Embryogenesis, to appear in IEEE Trans. Image Processing.

Zhang, J.W., Han, G.Q., & Wo Y., Image Registration based on Generalized and Mean Hausdorff Distances, Proceedings of the Fourth International Conference on Machine Learning and Cybernetics, Guangzhou, 2005.

List of Figures

1 Zebrafish embryo at the sphere (left) and shield (right) stage. The imaged volume is represented by the volume rendering. Scalar bar: 100μm 3

2 Voxel (box by black lines), point x_{ijk}^{100} (blue) on the "east" side where the gradient is approximated, voxel centers (red points) and points which are used for approximation of gradient in tangential direction (violet). 11

3 The original noisy data in volume rendering representation. The subvolume selected to construct the gold standard is shown in the small white bounding box. This subvolume consists of 71x100x28 voxels. On the top-right is the image histogram, the gray bar below the histogram shows the range of values between 25 and 30. For an isosurface representation of various ROI in this data set we refer also to Figures 11-12. 17

4 Comparison between the selected ROI of original data and its manual segmentation, chosen as gols standard. (a) Isosurface 25 in the ROI of original data depicted in blue. A red bounding box surrounds every object (nuclei and noise) inside the region. (b) Gold standard, represented in white. Every nucleus is surrounded by a white bounding box 19

5 Comparison between the selected ROI of original data and the gold standard. The plot of 11 nuclei of the gold standard (white) overlaps the corresponding component of isosurface 25 in the original data set (blue), for which we compute the mean Hausdorff distances. Each nucleus, both in original data and in the gold standard, is sourrounded by its bounding box (red and white, respectively). Small regions due to noise are not included in the computation of the mean Hausdorff distance and are not represented. 19

6 A 2D cut of original data and the cut of isosurface of value 28 of original and filtered data using same setting of filtering parameters ($K = 1, \sigma = 0.0001, \tau = 0.0001$) after 5 (a), 10 (b) and 15 (c) time steps. 20

7 Graphs of the original and filtered image intensities in a neighborhood of one of the nuclei from Figure 6 after 5 (a), 10 (b) and 15 (c) time steps. 20

8 Graphs of the mean Hausdorff distances for the original and filtered data using the same settings of parameters ($K = 1, \sigma = 0.0001, \tau = 0.0001$) after 5, 10 and 15 time steps (from top to bottom). 21

9 A 2D cut of original data with cut of the isosurface 28 of original and filtered data using the optimal values of parameters (cf. Table 5). 26

10 Graphs of the mean Hausdorff distances for the original data and data filtered using the optimal values of parameters (cf. Table 5). 27

11 Isosurface representation of original (a) and filtered data (by isosurface value 28) using optimal parameters (b-e). Parameters are given in Table 5. 29

12 Isosurface representation of original (a) and filtered data (by isosurface value 28) using optimal parameters,as shown in Table 5 (b-e). The Geodesic mean curvature flow is able to distinguish between two very close nuclei. 30

13 Graph of the MHD comparing original, geodesic mean curvature flow, tensor diffusion and Beltrami flow filtered data. 33

14 Plot of original and filtered (gmcf, tnd and Beltrami) image intensities in a neighborhood of one of the nuclei from Figure 6. 34

15 Isosurface of original (a) and filtered data (by isosurface value 28) comparing the geodesic mean curvature flow, the tensor diffusion and the Beltrami flow methods (b-d). The point of view is the same as in Figure 12. 34

16 Graph of the MHD comparing results obtained by Beltrami filtering with and without a Gaussian convolution. 35

17 Graphs of filtered image intensities in a neighborhood of one of the nuclei from Figure 6 to compare the Beltrami flow with and without a Gaussian convolution. 36

18 Isosurface of original (a) and filtered data (by isosurface value 28) comparing Beltrami flow with and without a Gaussian convolution. The point of view is the same as in Figures 12 and 15. 37

List of Tables

1 Errors in $L_\infty((0,T), L_2(\Omega))$-norm, EOC comparing numerical and exact solutions (38) and CPU time for one time step. 16

2 The mean Hausdorff distances and their standard deviation for the original data. Values are in μm. 22

3 The mean Hausdorff distances and their standard deviation in μm for the data filtered using the same settings of parameters after 5,10 and 15 time steps ($K = 1, \sigma = 0.0001, \tau = 0.0001$). 23

4 The number of regions for different isosurfaces found in the original and filtered data using the same settings of parameters ($K = 1, \sigma = 0.0001, \tau = 0.0001$). 24

5 The optimal parameters for different models. In the last row we present the computational times for such settings of parameters. 26

6 The mean Hausdorff distances and their standard deviation in μm for the filtered data using the optimal values of parameters (cf. Table 5). 27

7 The number of regions found in the original and filtered data using the optimal choice of parameters (cf. Table 5). 28

8 The number of connected regions found in original and filtered data using the optimal choice of parameters , as given in Table 5. 30

9 Comparison between geodesic mean curvature flow, tensor diffusion and Beltrami flow. Error expressed as the mean Hausdorff distance with its standard deviation. Distances in μm for original and filtered data. 33

10 The number of regions found in the original and filtered data comparing geodesic mean curvature flow, tensor diffusion and Beltrami flow. 35

11 Comparison of the Beltrami flow with and without a Gaussian convolution. Error expressed as the mean Hausdorff distance with its standard deviation. Distances in μm for original and filtered data. 36

12 The number of regions found in the original and filtered data comparing Beltrami flow with and without a Gaussian convolution. 37